

BIO-FLEXCLC

Flexible chemical looping combustion for combined heat and power production from biogenic residues with negative emission

HORIZON EUROPE GRANT AGREEMENT NUMBER: 101147904

Start date of project: 01/06/2024

Duration: 4 years

WP2

Improving process performance of Bio-FlexCLC

D2.2

CFD modelling of fuel reactors with packings

Topic: HORIZON-CL5-2023-D3-02-01
 Funding scheme: HORIZON-RIA
 Call identifier: HORIZON-CL5-2023-D3-02-01

Due date of deliverable: 31-08-2025	Actual submission date: 29-08-2025	
Document classification code: Bio-FlexCLC-WP02-D2.2-DLR-CERTH-29082025-V06		Prepared by: CERTH

Version	DATE	Changes	CHECKED	APPROVED
V01	12-08-2025	First Release	CERTH	George Kanellis
V02	21-08-2025	Feedback on the content	TUDA	Benjamin Michel
V03	22-08-2025	Feedback on the content	CTH	Nasrin Nemati
V04	22-08-2025	Feedback on the content	CSIC	Luis F. de Diego
V05	27-08-2025	Revised version	CERTH	George Kanellis
V06	29-08-2025	Final version	RISE	Amir Soleimani Salim

Funded by the European Union. Views and opinions expressed are however those of the author(s) only and do not necessarily reflect those of the European Union or the European Climate, Infrastructure and Environment Executive Agency (CINEA). Neither the European Union nor CINEA can be held responsible for them."

Dissemination Level		
PU	Public	X
SEN	Sensitive, limited under the conditions of the Grant Agreement	



D2.2 - CFD modelling of fuel reactors with packings

Proj. Ref.: Bio-FlexCLC-101147904
Doc. Ref.: Bio-FlexCLC-WP02-D2.2-DLR-CERTH-29082025-V06
Date: 29/08/2025
Page N°: 2 of 42

Content

1. EXECUTIVE SUMMARY	3
1.1. Description of the deliverable content and purpose	3
1.2. Brief description of the state of the art and the innovation brought	3
1.3. Deviation from objectives	3
2. METHODOLOGY	4
2.1. Models and Assumptions	4
2.1.1. Drag model.....	4
2.1.2. Reactions considered in the model.....	5
2.2. CFD Modelling of Packings	9
2.2.1. CFD approach.....	10
2.2.2. Initial simulations – Uniform porosity field	11
2.2.3. Simulations with non-uniform porosity	14
2.2.4. Reflections and outlook	16
2.3. Description of the considered cases.....	17
2.3.1. Chalmers University of Technology (CTH) 10 kW _{th} pilot plant.....	17
2.3.2. Spanish National Research Council (CSIC) 20 kW _{th} pilot plant.....	20
2.3.3. Technical University of Darmstadt (TUDA) 1 MW _{th} pilot plant.....	22
3. CFD MODELLING RESULTS	25
3.1. CFD modelling of the fuel reactor of CTH 10 kW _{th} pilot plant.....	25
3.2. CFD modelling of the fuel reactor of CSIC 20 kW _{th} pilot plant.....	32
3.3. CFD modelling of the fuel reactor of TUDA 1 MW _{th} pilot plant.....	35
4. CONCLUSIONS	40
5. ABBREVIATIONS	41
6. REFERENCES	42

1. EXECUTIVE SUMMARY

1.1. Description of the deliverable content and purpose

This report describes the work performed in Task 2.3. The aim of this task is to support the design of the fuel reactors that operate in the Bio-FlexCLC project, namely the 10 kW_{th} and 20 kW_{th} pilot plants at Chalmers University of Technology (CTH) and the Spanish National Research Council (CSIC), and the 1 MW_{th} pilot plant at Technical University of Darmstadt (TUDA). To this end, CERTH investigated the aforementioned reactors via computational fluid dynamics (CFD) modelling, with the goal of assessing the impact of design choices on gas–solid mixing, bubble formation, and reactor performance. All involved WP2 partners (CTH, CSIC, and TUDA) provided CERTH with the initial designs and operating points of their fuel reactors. Based on this input, CERTH performed CFD simulations to evaluate the designs, identify possible operational issues, and suggest options for improving efficiency. Where uncertainties existed regarding the operating conditions or the kinetics, conservative assumptions were applied, focusing on worst-case scenarios to ensure robust design assessment. For the CTH 10 kW_{th} bubbling bed reactor, several parametric simulations were performed, focusing on the solids circulation between the air and fuel reactors. Moreover, this reactor was selected in order to investigate the effect of packings. For the circulating bed reactors of CSIC and TUDA, parametric studies were carried out with varying bed inventory. In the absence of experimental data for packed bed configurations, for the CSIC and TUDA reactors, simulations were conducted to establish the baseline hydrodynamic and reactive behaviour without packings. The CFD studies conducted in this task are expected to provide valuable insights for reactor design and inform the planning of upcoming experimental activities within the project.

This report comprises four main paragraphs. The current paragraph states the main target of the performed work, describes briefly the performed numerical campaign, and closes by reporting the deviations (if any) from the initial objectives. Paragraph **"2.METHODOLOGY"** describes the numerical models that have been employed for the fuel reactor simulation, along with any relevant settings, assumptions and justifications. The main results of the numerical campaign are presented in the paragraph **"3.CFD MODELLING RESULTS"**. Finally, paragraph **"4 CONCLUSIONS"** summarizes the main findings of the CFD campaign.

1.2. Brief description of the state of the art and the innovation brought

- First CFD study addressing multiphase flow in fluidized bed reactors with solid packings, using a porous medium approximation for the packings' hydrodynamic effect.
- Multiphase Eulerian–Eulerian simulations combined with Lagrangian tracking of fuel particles.
- Adaptive use of drag models based on computational grid resolution:
 - Gidaspow drag model applied in fine grids.
 - EMMS-based model applied in coarser grids to account for mesoscale structures and better predict the pressure profile.
- Systematic parametric studies of hydrodynamics in the three pilot-scale fuel reactors of the Bio-FlexCLC project.
- The findings of this task provide critical guidance for reactor operation and scale-up while identifying key areas for further study.

The experience and models developed here will be further refined and validated in Task 4.7 of the Bio-FlexCLC project, where CFD predictions will be compared against experimental data, particularly for the TUDA reactor.

1.3. Deviation from objectives

There has been no deviation from the initial objectives that needs to be reported.

2. METHODOLOGY

2.1. Models and Assumptions

For the CFD simulations presented in this report, the ANSYS Fluent software package [1] is used. In all performed simulations, an Euler-Euler two fluid (TFM) model is applied to describe the two-phase flow of gases and oxygen carrier particles in the reactors. In addition, a Lagrangian approach is used to describe the fuel particles. This approach is followed since the number of fuel particles is much smaller than the number of oxygen carrier (OC) particles and therefore, fuel particles are present in low volume fractions in the domain. The two Eulerian phases, i.e. gas and solid particles, are treated as interpenetrating continua and their conservation equations are solved in the Eulerian reference frame. In TFM, the interactions between the particles comprising the solid phase are modelled through the inclusion of closure terms based on the kinetic theory of granular flows (KTGF). In particular, the solid pressure and the bulk viscosity is calculated according to Lun [2], the shear viscosity according to Gidaspow [3], and the radial distribution function according to Lun and Savage [4]. In addition, the frictional packing limit is set at 0.5, over which an additional frictional viscosity is added according to the model of Schaeffer [5], while a frictional pressure is added according to Johnson and Jackson's model [6].

Regarding the fuel particles, a force balance equation according to Newton's 2nd law is solved in the Lagrangian reference frame, i.e.:

$$m_p \frac{d\vec{u}_p}{dt} = \frac{m_p}{\tau_r} (\vec{u} - \vec{u}_p) + m_p \frac{\vec{g}(\rho_p - \rho)}{\rho_p}, \quad (1)$$

where m_p is the mass of the particle, \vec{u} is the velocity of the fluid phase, \vec{u}_p is the particle velocity, ρ is the fluid density, ρ_p is the particle density, $\frac{m_p}{\tau_r} (\vec{u} - \vec{u}_p)$, is the drag force and τ_r is the particle or droplet relaxation time given by:

$$\tau_r = \frac{\rho_p d_p^2}{18\mu} \frac{24}{C_d Re}, \quad (2)$$

where d_p is the diameter of the particle, μ is the dynamic viscosity of the fluid, C_d is the drag coefficient and Re is the Reynolds number defined as:

$$Re = \frac{\rho d_p |\vec{u} - \vec{u}_p|}{\mu}, \quad (3)$$

Regarding the heat transfer, due to the relatively uniform temperature field in the fuel reactors, isothermal simulations are applied. The applied model is based on ANSYS Fluent (v22.1) [1], and the applied governing equations can be found in [7].

2.1.1. Drag model

In multi-phase flows, in the case of bubbling or circulating beds, one important aspect of a developed model is the choice of the drag model. In the present work, the selection of the drag model depended on the computational grid. Regarding the computational grid for such flows, an important parameter is the average cell size to particle diameter ratio, D_{cell}/d_p . In general, it is reported that for an accurate prediction of the momentum exchange between the coupled phases, an equivalent cell size of at less than 20 times the average particle diameter is required [8], [9].

For the batch scale reactor, as well as for the CTH 10 kW_{th} fuel reactor, where the computational domain is small, a relatively fine mesh was used, giving a D_{cell}/d_p ratio of about 20. Under these conditions, the homogeneous Gidaspow drag model was applied. Conversely, in the CSIC and TUDA reactors the cell size to particle diameter ratio was much higher, 50 for the CSIC reactor and 330 for the TUDA case.

Therefore, for these reactors, the sub-grid EMMS model is used to calculate the gas-solid drag coefficient. This highly advanced model takes into account the meso-scale structural effect on the calculation of the drag coefficient in each computational cell, through a heterogeneity index, H_d , which is derived from the solution of a set of analytical, empirical and semi-empirical equations for specific values of the gas-solid slip velocity, u_{slip} , varying from 0.2 m/s to 5 m/s, and for discrete values of the gas volume fraction ε_g within the range of ε_{mf} to ε_{max} . ε_{mf} is the voidage at minimum fluidization conditions and $\varepsilon_{max} \cong 0.9997$, a voidage over which the flow is considered uniform ($H_d = 1$) due to the fact that particles are effectively absent. The calculated H_d index is then incorporated into the TFM model through a user-defined function and the drag (F_{EMMS}) is calculated as:

$$F_{EMMS} = F_{Wen\&Yu}/H_d, \quad (4)$$

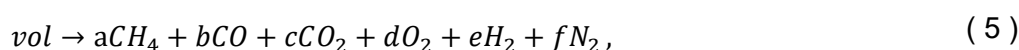
where $F_{Wen\&Yu}$ is the drag according to Wen and Yu formulation. Validation of this type of drag model has been achieved by our research group for a wide range of operating conditions, for both Geldart A and Geldart B particles. More details on the EMMS approach can be found in [9], [10], [11].

2.1.2. Reactions considered in the model

An essential aspect of the model is the set of chemical reactions involved. In the fuel reactor of a Chemical Looping plant, fuel oxidation occurs indirectly through the reduction of the solid oxygen carrier. In this study, the fuel is solid biomass (pellets or chips), and the oxygen carrier is also a solid phase. The biomass first undergoes devolatilization, releasing volatiles, while the remaining char is gasified. The combustible gases produced subsequently react with the oxygen carrier, leading to its reduction. The system involves a complex network of heterogeneous and homogeneous reactions, which, for modeling purposes, are grouped into three categories: biomass transformations, heterogeneous reactions with the oxygen carrier, and homogeneous gas-phase reactions. The following subsections describe each category.

2.1.2.1. Biomass Transformations

The transformations the biomass particles undergo are presented in Figure 1. Initially, they undergo boiling/evaporation until they dry. Then they lose the volatiles under the so-called devolatilization process. Then the char undergoes gasification under H_2O and CO_2 gases that are present in the fuel reactor. The default laws in Ansys/Fluent for the “combustible” particle are used. Here, the setup of the biomass transformation will be briefly described. More information about the ANSYS Fluent laws and how they are applied can be found in [7]. In ANSYS/Fluent the product of the devolatilization is set to be a gaseous mixture of volatiles. In particular, the following transformation is considered:



Looking at Eq. (5), we see that this equation contains six unknowns (a–f). To solve for them, we apply four elemental balances (C, H, O, N) and a total mass balance. Instead of imposing the energy balance as an exact constraint, it is treated as an optimization target. This avoids infeasible solutions that may arise from over-constraining the system. The energy content of the fuel volatiles is known, and the combustion energy of the gaseous mixture on the right-hand side can be calculated once its composition is fixed. A Python optimization algorithm determines the molar fractions by satisfying the elemental and mass balances, while minimizing the difference in energy between the original volatiles and the product gases. Typically, the energy content of the gas mixture is slightly higher than that of the original volatiles. In such cases, devolatilization is considered endothermic, with reaction enthalpy equal to the energy difference. This ensures the overall energy balance of the process is maintained.

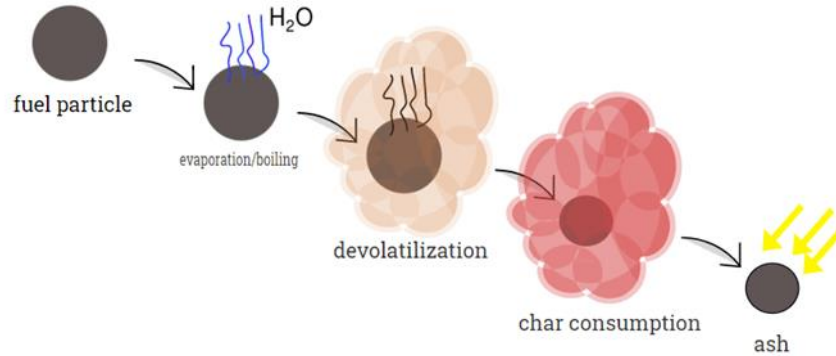


Figure 1. Transformation of a biomass particle.

Following discussions with project partners, the selected fuels for the CFD simulations were:

- CTH 10 kW_{th} fuel reactor: Black pellets
- CSIC 20 kW_{th} fuel reactor: Pine wood pellets
- TUDA 1 MW_{th} fuel reactor: Wood pellets

Ultimate and proximate analyses of these fuels, along with their lower heating values (LHV), are summarized in Table 1. Other fuels may also be tested experimentally by the project partners.

Table 1. Fuel characteristics considered for the different fuel reactors.

Fuel	Black pellets	Pine wood pellets	Wood pellets
	CTH	CSIC	TUDA
Proximate analysis			
Moisture (wt%)	6.9	7.5	7
Ash (wt%)	0.3	0.2	1.86
Volatiles (wt%)	74.2	77.1	78.86
Fixed Carbon (wt%)	18.7	15.1	12.28
LHV (kJ/kg)	18640	17042	18410
Ultimate analysis			
C (wt%)	49.8	47.8	48.03
H (wt%)	5.6	5.3	5.833
N (wt%)	0.09	0.2	0.355
O (wt%)	37.4	39.1	36.91

Regarding the gasification with CO₂ or H₂O, the following reactions are considered (Boudouard and carbon-steam reaction):



The rate used for these reactions can be written as follows:

$$R_S = AT^\beta \exp\left(-\frac{T_a}{T} - a\right) \prod_{i=1}^n [c_i]^{\eta_i} \cdot m_p X_{char}, \tag{7}$$

where A is the pre-exponential factor expressed in (m³ⁿ/molⁿ/K^β/s), T is the particle temperature in (K), β is the temperature exponent (-), T_a is the activation temperature (K), a is a dimensionless constant (-), c_i

is the molar concentration of the gaseous reactant in the i -th reaction expressed in (mol/m^3), m_p is the current particle mass (kg) and X_{char} is the current char mass fraction. The definition of the parameters above and which of these heterogeneous reactions are taken to account in each fuel is based on [12] and can be seen in Table 2.

Table 2. Gasification reactions.

	Reactions	A ($\text{m}^{3n}/(\text{s}\cdot\text{mol}^n\cdot\text{K}^\beta)$)	Ta (K)	α	β	η
G1	$\text{C} + \text{CO}_2 \rightarrow 2\text{CO}$	7.63E+01	22645	0	1	1
G2	$\text{C} + \text{H}_2\text{O} \rightarrow \text{CO} + \text{H}_2$	7.63E+01	22645	0	1	1

2.1.2.2. Heterogeneous Reactions with the Oxygen Carrier

From a fuel reactor modeling perspective, the most important reactions are the heterogeneous reactions between the combustible gases (released from devolatilization or gasification) and the oxygen carrier, which oxidizes the gases while reducing the carrier. Ilmenite was selected as the oxygen carrier for the simulations. The material mainly consists of iron and titanium oxides (FeTiO_3 , Fe_2TiO_5 , Fe_2O_3 , TiO_2 , and Fe_3O_4). In the following, the oxygen carrier in its oxidized form is denoted as M_O , and in its reduced form as M . In particular, the heterogeneous reactions considered are:



However, after discussions with partners, there were some differences concerning the properties of the oxygen carrier particles that will be used, namely the mean particle diameter, the density of the material in its oxidized form, and the oxygen transport capacity, R_{OC} . These properties are summarized in Table 3. The mean particle diameter is calculated from the following relation from Kunii and Levenspiel [13]:

$$\bar{d}_p = \frac{1}{\sum_i \frac{f_k}{d_{pk}}}, \quad (11)$$

where f_k is the mass fraction of particles with diameter equal to d_{pk} . From Table 3, it can be observed that the TUDA case have a much finer oxygen carrier.

Table 3. Properties of the considered Oxygen Carrier particles.

	CTH Batch reactor	CTH 10 kW _{th} fuel reactor	CSIC cases	TUDA cases
\bar{d}_p (μm)	179	250	170	67
ρ_p (kgm^{-3})	2730	2730	3200	3710
R_{OC} (wt%)	3.3	3.3	3.3	3.7

Regarding the heterogeneous reaction rate for the reactions described in Eqs. (8), (9) and (10), it is obtained from the work of Abad et al [14]. The conversion X of the oxygen carrier is defined as:

$$X = \frac{m_0 - m}{R_{OC} m_0}, \quad (12)$$

where m and m_0 are the current and the fully oxidized masses of the oxygen carrier, respectively, and R_{OC} is the oxygen carrier oxygen transport capacity. According to Abad [14] the conversion is described by the following:

$$\frac{t}{\tau_{chr}} = 1 - (1 - X)^{1/3}, \quad (13)$$

where τ_{chr} is given by

$$\tau_{chr} = \frac{\rho_m \cdot r_g}{\bar{b} \cdot k_s \cdot C_g^n}, \quad (14)$$

where ρ_m (molm^{-3}) is the molar density, r_g (m) is the grain radius, \bar{b} is the average stoichiometric coefficient for reaction of solid with reacting gas in mol metal oxide per mol of gas, k_s is the chemical kinetic constant calculated by an Arrhenius expression ($k_s = k_{s0} e^{-E_{chr}/(R_g T)}$), C_g is the average gas concentration in molm^{-3} and n is the reaction order. Finally, by differentiating Eq. (13) with respect to time, the rate of conversion can be expressed as:

$$\frac{dX}{dt} = \frac{3}{\tau_{chr}} (1 - X)^{2/3}, \quad (15)$$

All parameter values and further details for the rate calculation can be found in [14].

2.1.2.3. Homogeneous Gas-Phase Reactions

In this study, the set of homogeneous reactions includes: a) the water-gas shift reaction, b) the carbon monoxide oxidation, c) the hydrogen oxidation and d) the methane oxidation. The reactions with oxygen have been added since there is a very limited amount of oxygen coming from devolatilization. This is consumed fast by reacting with combustible volatiles. The reaction rate is calculated from the following relations:

$$\hat{R}_{i,r} = (v''_{i,r} - v'_{i,r}) \left(k_{f,r} \prod_{j=1}^N [C_{j,r}]^{\eta'_{j,r} + \eta''_{j,r}} \right), \quad (16)$$

$$k_{f,r} = A_r T^{\beta_r} e^{-T_a/T}, \quad (17)$$

where $v''_{i,r}$ is the stoichiometric coefficient for product i in reaction r , $v'_{i,r}$ is the stoichiometric coefficient for reactant i in reaction r , $\eta'_{j,r}$ and $\eta''_{j,r}$ are the rate exponents for reactant and product species j in reaction r , and $C_{j,r}$ is the molar concentration of species j in reaction r (in kmol/m^3). Furthermore, A_r is the pre-exponential factor for the reaction r expressed in ($\text{kmol}^{1-n}/\text{s}/\text{m}^{3-3n}$), where β_r is the temperature exponent, which is zero in our case, and T_a is the activation temperature (K). The required coefficients for the rate calculation are found from [12] and reported in Table 4. Looking at the first two rows of Table 4, it is noted that the water-gas shift reaction, which is reversible, is passed as two irreversible ones in ANSYS/Fluent.

Table 4. Homogeneous reactions.

	Reactions	A (kmol ^(1-η_1) /m ^{3(1-η_1)} /s)	T _a (K)	η_1	η_2	η_3
R1	$\text{CO} + \text{H}_2\text{O} \rightarrow \text{CO}_2 + \text{H}_2$	2.75E+6	10055	0.5	1	-
R2	$\text{CO}_2 + \text{H}_2 \rightarrow \text{CO} + \text{H}_2\text{O}$	1.04E+8	14010	1	0.5	-
R3	$\text{CO} + 0.5\text{O}_2 + \text{H}_2\text{O} \rightarrow \text{CO}_2 + \text{H}_2\text{O}$	2.24E+12	20086	1	0.25	0.5
R4	$\text{H}_2 + 0.5\text{O}_2 \rightarrow \text{H}_2\text{O}$	9.87E+8	3728	1	1	-
R5	$\text{CH}_4 + 2\text{O}_2 \rightarrow \text{CO}_2 + 2\text{H}_2\text{O}$	2.12E+11	24380	0.2	1.3	-

2.2. CFD Modelling of Packings

To explore the feasibility of using a porous media approach to model solid packings in bubbling fluidized beds, we simulated the CTH lab-scale batch reactor, for which detailed experimental results are available in [15]. This reactor is particularly valuable as a reference, since it is the only configuration among the project-related cases with published experimental data for configurations with packings.

The experimental setup, shown in Figure 2, involved packing the batch-scale reactor up to 1m height. Two different types of packing material are tested: Hiflow stainless-steel pall ring and RMSR stainless-steel thread saddle. Both have the same nominal size (25 mm) and similar nominal voidage (0.96 for RMSR and 0.95 for Hiflow packings). Two fuel types were used in the tests: pure CO and a 50/50 syngas mixture (CO/H₂). Different oxygen carrier inventories were studied, quantified by the settled bed height, which varied from 10 cm – 60 cm.

The procedure involved oxidizing the ilmenite particles under air at 21 L_n/min during heating to a target temperature of 840 °C. Once the temperature stabilized, the reactor was purged with N₂, and then the fuel gas mixture (15 L_n/min CO or syngas + 6 L_n/min N₂) was introduced. The duration of fuel injection was calculated so that the injected fuel would suffice, if completely converted, to ensure a 0.8% reduction of the ilmenite inventory. According to the experimental results, the packings helped improve the fuel conversion achieved at a certain settled-bed height. Or equivalently, it was shown that a certain conversion can be achieved at a lower inventory, i.e., with a lower settled height, when packings are used. The reason was shown to be the decrease in the average bubble size when packings are used. This increased the mixing in the reactor and the mass transfer of fuel to the emulsion phase of the oxygen carrier, where the heterogeneous reduction reactions take place.

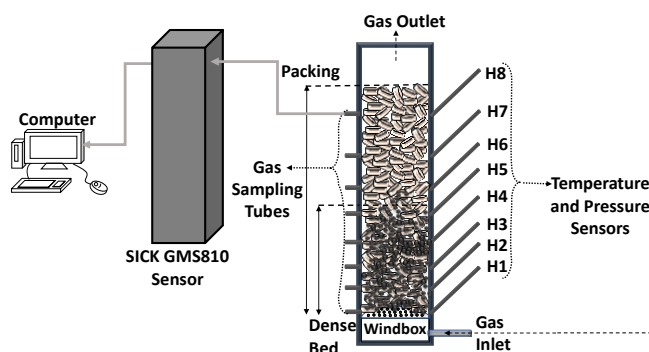


Figure 2. Lab-scale reactor used in batch experiments. Figure is taken from [15].

For this work, we focused on the RMSR packing cases with inventory corresponding to the experimental cases with a settled bed height of 30cm. CERTH received all the respective raw experimental data from CTH.

Figure 3 shows the conversion achieved versus time for the case of 30 cm settled bed height when using RMSR packings and no packings. In the actual experiment there is always some lag between the time point when the fuel is started and when it starts entering the domain with the said flux (16 L_n/min). This is obvious when looking at the figure, since at the first 40 plus seconds there is no conversion, and, slowly, the conversion slope increases until it achieves a constant slope for a considerable amount of time, before the slope starts decreasing again at the end of the experiment. Therefore, for comparison with CFD, we considered the stable part of the experiment. Regarding this specific part, it was calculated that the case with packings had an 20% increase of the conversion rate, compared to the no packing case (see Figure 3).

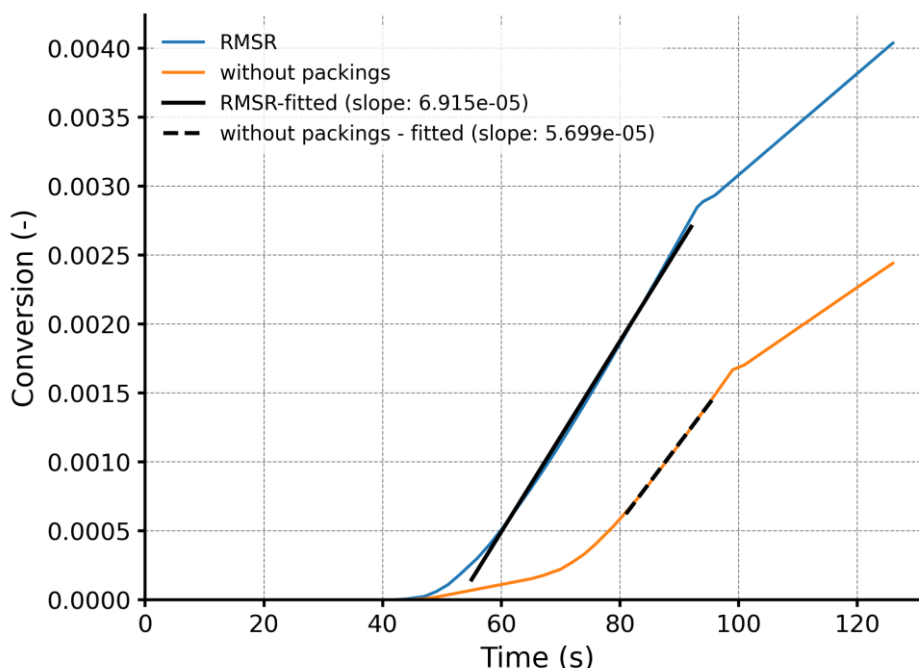


Figure 3. Experimental results of the reduction stage with RMSR packings and without packings for a settled height of oxygen carrier of 30 cm.

2.2.1. CFD approach

The geometry and mesh are shown in Figure 4. The grid consisted of approximately 110,000 hexahedral cells, designed to ensure a cell size to particle diameter ratio of ~20, allowing consistent use of the Gidaspow [3] drag model.

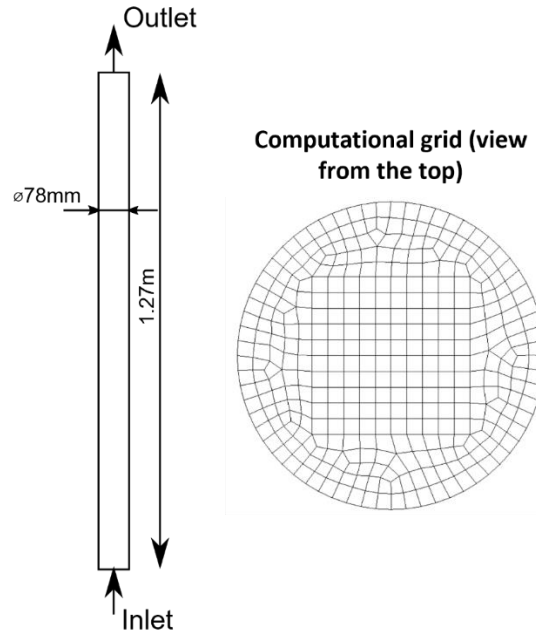


Figure 4. Geometry and view from the top of the computational grid applied.

The CFD simulations were configured to reproduce the reduction phase of the experiment. The simulation was isothermal with a temperature of 840 °C. The reactor was initially filled with N₂, and at t = 0, a mixture of CO and N₂ (mass flux = 0.000437 kgs⁻¹; 71.4% CO, 28.6% N₂ by mass) was injected at the inlet. Atmospheric pressure was imposed at the outlet (101325 Pa). The boundary conditions are summarized in Table 5.

Table 5. Boundary conditions applied to the lab-scale CTH reactor.

Boundary patch	Boundary condition	
	Gas/Solid fluxes	Composition - Mass fractions
Inlet	$m_{gas} = 0.000437kgs^{-1}$	$Y_{CO} = 0.714$ $Y_{N_2} = 0.286$
Outlet	Pressure outlet (p = 101325 Pa)	

2.2.2. Initial simulations – Uniform porosity field

In CFD, the RMSR packings are modelled using a porosity field. Initially, a uniform porosity corresponding to the nominal voidage of the RMSR elements is used in the region of the packings (up to 1m height). Figure 5 presents the cumulative CO₂ exiting the reactor's outlet and the mass-based conversion of the oxygen carrier both as predicted by CFD and measured experimentally. It also shows the corresponding experimental results with and without packings. The mass-based OC conversion is defined as:

$$X = 1 - \frac{m}{m_{ox}}, \quad (18)$$

where m_{ox} is the mass of the oxygen carrier in its fully oxidized form.

To facilitate comparison, the CFD results were time-shifted so that the onset of conversion aligns with the experimental curves. This is a common practice when synchronizing transient data. As seen in Figure 5, the experiments clearly show an acceleration in conversion with the use of packings, which leads to a higher cumulative CO₂ release at a given time. However, the CFD predictions exhibit almost identical behavior with and without packings. This discrepancy likely arises because the high porosity of the

packings results in minimal and also uniform hydrodynamic resistance when a uniform porosity is applied. As a result, the flow pattern is not significantly altered, and bubble breakup is not observed.

As described in Section 2.1.2.2 of the Methodology, the Abad reaction rate [14] was initially used for modelling the heterogeneous reduction of the oxygen carrier. However, as shown in Figure 5, the CFD simulation without packings predicted a significantly faster conversion than the corresponding experiment. To investigate the sensitivity of the model to reaction kinetics, a second simulation was performed using 10% of the Abad rate [14].

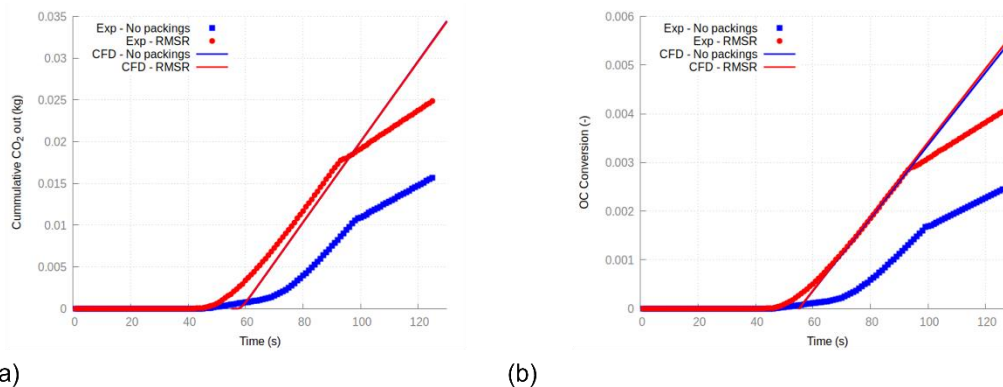


Figure 5. Cumulative CO₂ leaving the reactor (a) and mass-based OC conversion (b), using the nominal Abad rate [14].

The cumulative CO₂ release and OC conversion for this case are shown in Figure 6. This adjustment is justified, as heterogeneous reaction rates are highly dependent on particle-specific properties (e.g., size distribution, internal porosity). So, tuning the pre-exponential factor of a certain model is a common approach to improve agreement with experimental data. Even after this adjustment, however, CFD predictions with and without packings remain nearly identical (Figure 6). This suggests that the current porous media model, particularly with a uniform porosity, is not sufficient to capture the experimentally observed enhancement in conversion caused by the packings.

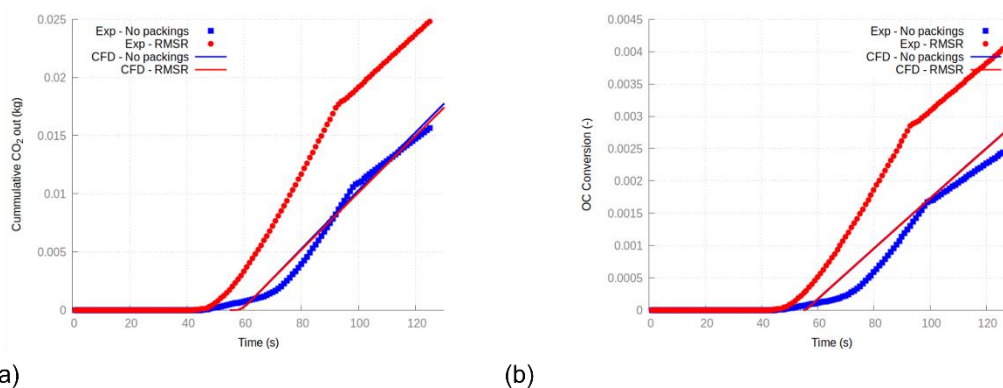


Figure 6. Cumulative CO₂ leaving the reactor (a) and mass-based OC conversion (b), using 0.1× Abad rate [14].

Figure 7 shows instantaneous contours of the solid volume fraction in a vertical cross-section of the reactor (parallel to the reactor axis of symmetry), for cases with and without packings. The flow structures and bubble sizes appear similar, again suggesting that the uniform porosity model fails to reproduce the experimentally observed bubble breakup.

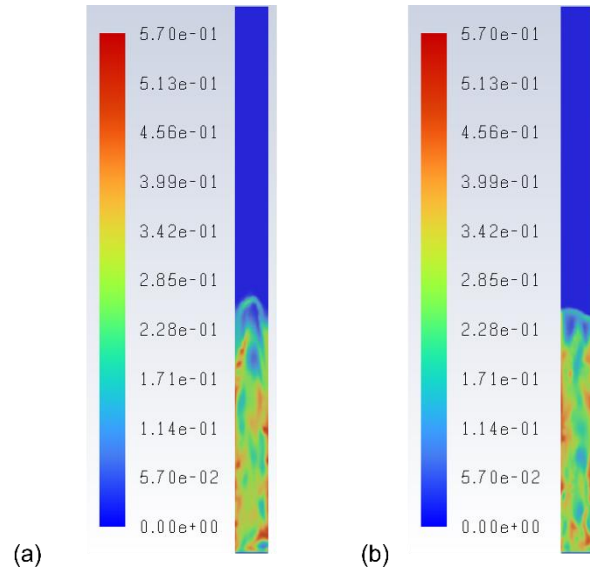


Figure 7. Contours of solid volume fraction for cases without (a) and with (b) packings.

Since the instantaneous figures do not visually allow to accurately quantify the change in bubble size, appropriate correlations [15] were used to calculate an average bubble size based on the CFD results. From CFD data we can easily calculate the time-averaged bubble fraction δ and the time-averaged voidage ϵ_f of the bed. These can be readily calculated from the CFD solution based on the volume fraction of each computational cell. Regarding the bubble fraction a threshold of solid volume fraction < 0.3 was adopted to define the bubble face, following similar approaches in [16], [17]. After having calculated δ and ϵ_f we can subsequently employ the following equations:

$$\delta = \frac{u_0 - u_{mf}}{u_b - u_{mf}}, \quad (19)$$

$$\frac{\epsilon_f - \epsilon_{mf}}{1 - \epsilon_{mf}} = \frac{u_0 - u_{mf}}{u_b - u_{mf}}, \quad (20)$$

In the above equations, u_0 is the superficial fluidization velocity, u_{mf} is the minimum fluidization velocity, u_b is the rise velocity of bubbles, ϵ_{mf} is the voidage at minimum fluidization velocity and ϵ_f is the average bed voidage. Here $u_{mf} = 0.01656 \text{ m/s}$ is calculated from the following relation found in Kunii & Levenspiel [13], similar to [15] :

$$\frac{d_p u_{mf} \rho_g}{\mu} = \left[(28.7)^2 + 0.0494 \left(\frac{d_p^3 \rho_g (\rho_s - \rho_g) g}{\mu^2} \right) \right]^{1/2} - 28.7 \quad (21)$$

Then, $\epsilon_{mf} = 0.5176$ is calculated based on [15] from:

$$\frac{1.75}{\epsilon_{mf}^3 \Phi_s} \left(\frac{d_p u_{mf} \rho_g}{\mu} \right)^2 + \frac{150(1 - \epsilon_{mf})}{\epsilon_{mf}^3 \Phi_s^2} \left(\frac{d_p u_{mf} \rho_g}{\mu} \right) = \frac{d_p^3 \rho_g (\rho_s - \rho_g) g}{\mu^2} \quad (22)$$

In addition, u_b can also be approximated as a function of the average bubble size as:

$$u_b = 0.711 \sqrt{g d_b} \quad (23)$$

By combining Eqs (19) with (23), we can calculate the average bubble size based on δ , i.e. $d_{b,\delta}$, while by combining Eqs (20) with (23), we can calculate the average bubble size based on ε_f , i.e. d_{b,ε_f} . Table 6 summarizes the predicted bubble fraction and average bed voidage as well as the estimated average bubble sizes for all CFD cases, with and without packings, and for both reaction rates. Looking at the bubble diameter estimates, it can be seen that the size of the bubbles in the CFD solution is not affected by the presence of packings. Regarding the values of bubble sizes are unrealistically large (greater than the reactor diameter). The reason is that Eqs. (19) and (23) are approximate and not always consistent with experimental observations. (see Kunii [13] (page 155)). Thus, the values should be regarded as **qualitative indicators for comparing trends between cases**, rather than precise bubble size predictions.

Table 6. Predicted average bubble fraction and bed voidage from CFD simulations and estimated average bubble sizes based on CFD results.

Case ID	Packings	Reaction rate	δ	ε_f	$d_{b,\delta}$ (m)	$d_{b,\varepsilon_{mf}}$ (m)
NoPack-Abad	No	Abad	0.366	0.669	0.1249	0.1687
UniformPorosity- Abad	Yes	Abad	0.346	0.667	0.1391	0.1726
NoPack-0.1Abad	No	0.1 × Abad	0.356	0.668	0.1321	0.1717
UniformPorosity- 0.1Abad	Yes	0.1 × Abad	0.368	0.675	0.1237	0.1565

2.2.3. Simulations with non-uniform porosity

To investigate further, we introduced a spatially varying porosity field using a trigonometric function with a spatial period of 25 mm (matching the packing size). The contour of the applied porosity field is plotted in Figure 8. The simulation results obtained using this non-uniform porosity field are compared to both experimental data and previous CFD results without packings. Figure 9 (a) presents the cumulative CO₂ leaving the reactor, while Figure 9 (b) shows the corresponding mass-based conversion of the oxygen carrier, using the nominal Abad reaction rate [14]. A similar comparison is provided in Figure 10, where the reduced rate (0.1 × Abad) is used to account for possible kinetic limitations observed in prior simulations.

From these figures, especially the conversion plots in Figure 9 (b) and Figure 10 (b), it can be observed that modeling the RMSR packings via a non-uniform porosity field results in a moderate acceleration (~5%) in OC conversion rate compared to the no-packings case. This represents a clear improvement over the uniform porosity model discussed in Section 2.2.2., which failed to produce any noticeable enhancement. However, the experimentally observed conversion rate speed-up is approximately 20%, which is not fully captured by the current CFD approach.

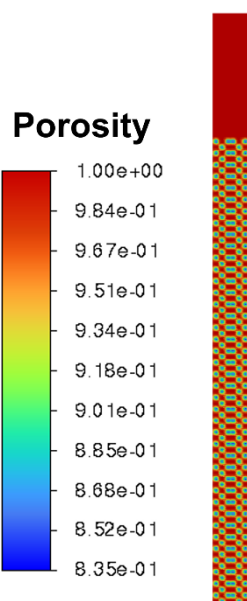


Figure 8. Contour of the applied porosity field based on a trigonometric function.

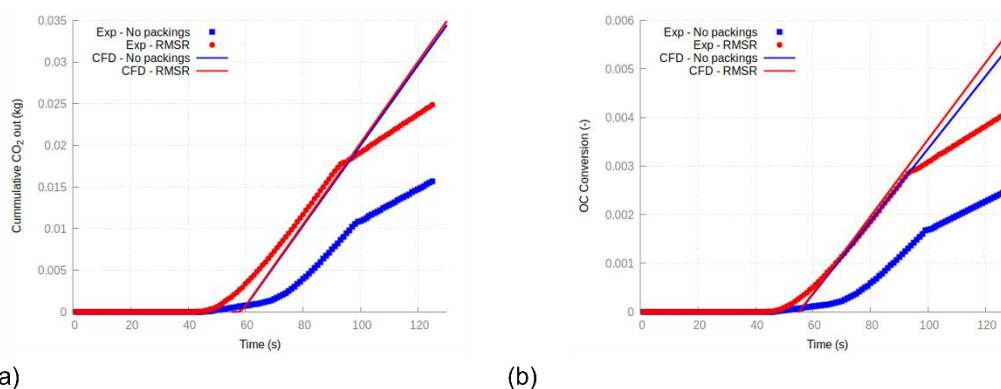


Figure 9. Cumulative CO₂ leaving the reactor (a) and mass-based OC conversion (b), using the nominal Abad rate. The presented CFD results incorporate a non-uniform porosity shown in Figure 8.

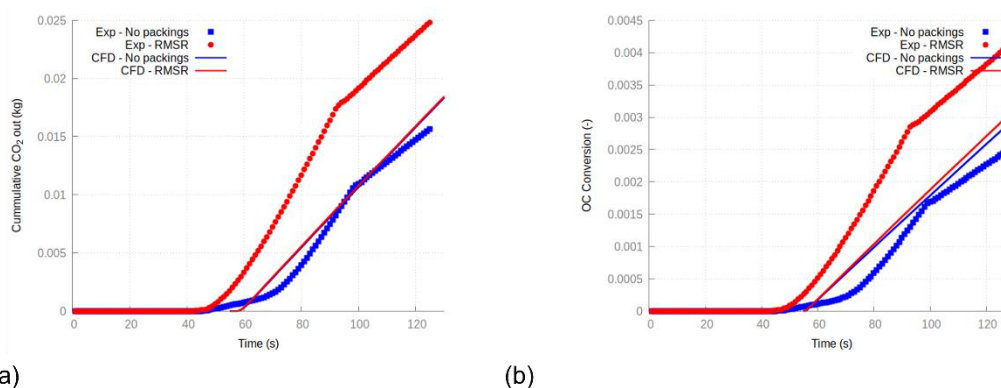


Figure 10. Cumulative CO₂ leaving the reactor (a) and mass-based OC conversion (b), using 0.1× Abad rate. The presented CFD results incorporate a non-uniform porosity shown in Figure 8.

Further insight into the hydrodynamics is provided by the solid volume fraction contours shown in Figure 11, which compares the case without packings (Figure 11 (a)) with the one including packings implemented

through the non-uniform porosity field (Figure 11 (b)). The inclusion of packings results in smaller bubbles and a more homogeneous distribution of solids, indicating that the flow structure is significantly affected.

To quantify these visual observations, the average bubble fraction and the average bed voidage is calculated from CFD. Then, the average bubble size was estimated using the empirical relations introduced in Eqs. (19) - (23). The resulting values are summarized in Table 7. Compared to the results in Table 6, which correspond to the no-packings and uniform porosity cases, the simulations using the non-uniform porosity field show a clear reduction in bubble size. This is consistent with the observed improvement in OC conversion, supporting the idea that the introduction of spatial porosity variation improves the CFD model’s ability to reflect the experimental trends—albeit not fully.

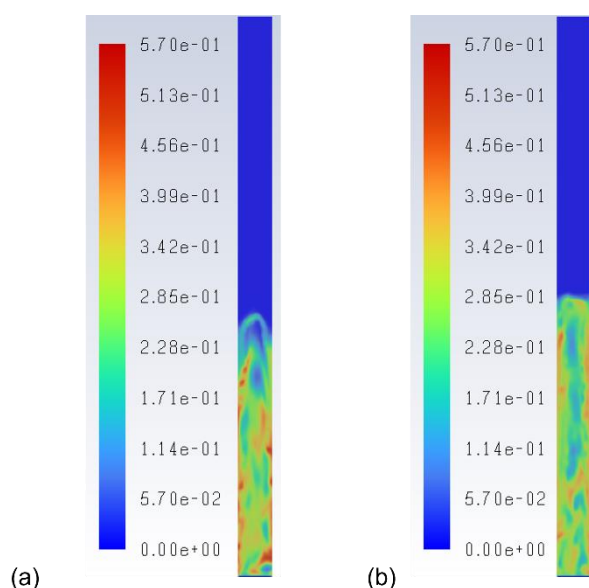


Figure 11. Contours of solid volume fraction at a case without (a) and with (b) packings incorporated as a non-uniform porosity field (see Figure 8).

Table 7. Predicted average bubble fraction and bed voidage from CFD simulations and estimated average bubble sizes based on CFD results.

Case ID	Packings	Reaction rate	δ	ϵ_f	$d_{b,\delta}$ (m)	$d_{b,\epsilon_{mf}}$ (m)
NonUniformPorosity-Abad	Yes	Abad	0.487	0.703	0.0716	0.1140
NonUniformPorosity-0.1Abad	Yes	0.1 × Abad	0.456	0.698	0.0813	0.1194

2.2.4. Reflections and outlook

This exercise illustrates both the potential and limitations of porous media modeling for packed beds in bubbling fluidized regimes. While qualitative effects such as bubble size reduction can be observed, the quantitative improvement in conversion is not well predicted. This suggests that further CFD research is required in this area, potentially involving:

- More sophisticated sub-grid models
- Hybrid approaches combining porous zones with resolved elements
- Direct inclusion of packing geometry (e.g. via resolved STL (stereolithography file format) or lattice structures)

However, such developments are beyond the scope of the current technical project, whose objective is to model fuel reactor configurations at pilot plant scale in support of design — not to develop new porous media models.

The porous media approach was applied as planned, and its limitations have been clearly identified. For the remainder of this work, focus is placed on the three main fuel reactor configurations (CTH 10 kW_{th}, CSIC 20 kW_{th}, TUDA 1 MW_{th}), which are to be modeled according to the designs provided by the experimental partners.

2.3. Description of the considered cases

In this section the simulations of the fuel reactors that will be used in this project are described, namely the 10 kW_{th}, 20 kW_{th} and 1 MW_{th} fuel reactors of the pilot plants of CTH, CSIC and TUDA, respectively.

2.3.1. Chalmers University of Technology (CTH) 10 kW_{th} pilot plant

The CAD of the fuel reactor of the 10 kW_{th} pilot plant at Chalmers can be seen in Figure 12. In this figure, the several inlets/and outlets are named and shown. The fuel reactor contains a volatile distributor (VD) to more evenly distribute the volatiles of the fuel in the bubbling bed of oxygen carrier (OC) particles. Volatiles are introduced through 76 small ports, arranged as 19 ports on each of the four vertical walls.

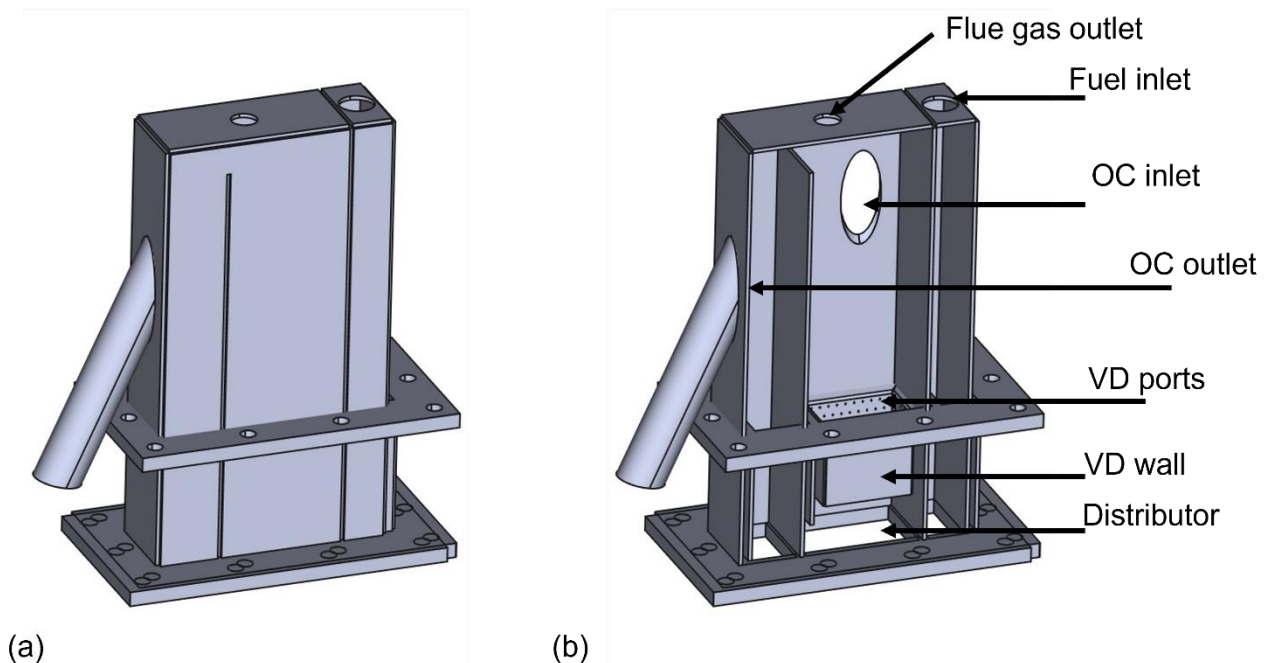


Figure 12. External view of the 10 kW_{th} fuel reactor: (a) with the front wall in place; (b) with the front wall removed to reveal the internal configuration.

The reactor geometry and mesh were prepared using the ANSYS platform [18]. A cell-to-particle diameter ratio of 20 was chosen to ensure reliable predictions from the Gidaspow drag model. Due to the very small size of the volatile distributor ports, they were simplified in the geometry as a single slit opening with equivalent total area to facilitate mesh generation. Additionally, all circular and elliptical inlets/outlets were replaced with rectangular shapes to further simplify the meshing process. The resulting computational grid, consisting of approximately 70,000 hexahedral cells, is shown in Figure 13.

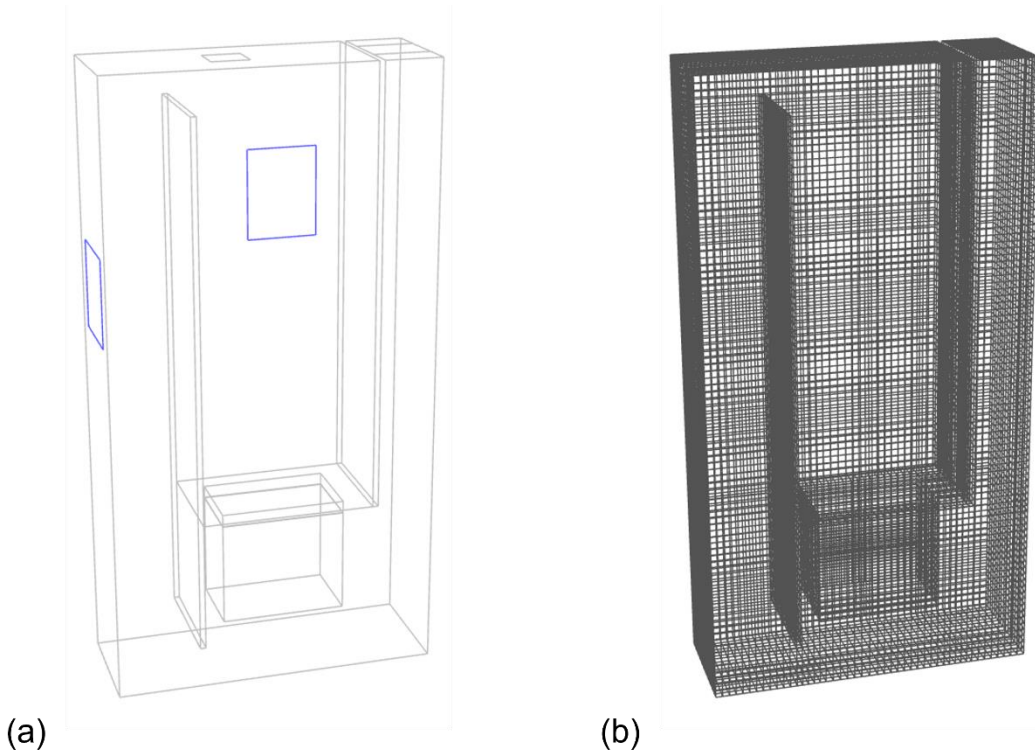


Figure 13. Geometry used for the CFD simulations (a), and corresponding computational mesh (b).

2.3.1.1. Operating and boundary conditions

The setup of the 10 kW_{th} fuel reactor simulations was based on the experimental configuration developed by the project partners, which is, in turn, based on previous experiments described in [19]. The simulations are isothermal, with the reactor temperature fixed at 975 °C. The fuel used is black pellets (BP), with a mass flux of 1.931 kg/h, corresponding to a thermal input of 10 kW. Steam is used as a fluidization medium, injected from the bottom of the reactor at a rate of 26 g/min.

However, one parameter needed was not available, which is the OC entering the reactor. To estimate the required circulation of the oxygen carrier (OC), an oxygen mass balance is considered at equilibrium. The relevant equation is:

$$\dot{m}_{s,in} Y_{M_O,in} R_{ox} - \dot{m}_{s,out} Y_{M_O,out} R_{ox} = M_{RO}, \quad (24)$$

where $\dot{m}_{s,in}$, $Y_{M_O,in}$, and $\dot{m}_{s,out}$, $Y_{M_O,out}$ are the mass flux of OC and the mass fraction of the oxidized species (M_O) at the OC inlet and the OC outlet, respectively. $R_{ox} = 0.033 \text{ kg O}_2 / \text{kg M}_O$ is the mass of removable oxygen per kg of oxidized species. Finally, M_{RO} is the mass of oxygen per second that reacts with fuel in the reactor. The minimum amount of circulation should be such that the amount of removable oxygen entering the reactor from the OC inlet suffices to completely oxidize the amount of fuel input in the reactor. To determine the minimum required circulation of OC, we consider the following:

- The OC entering the fuel reactor is completely oxidized (i.e. $Y_{M_O,in} = 1$)
- The OC leaving the reactor is in reduced state ($Y_{M_O,out} < 1$). For the calculation of the lower limit on circulation it is considered that ($Y_{M_O,out} = 0$)
- For complete fuel oxidation the amount of the required oxygen is $M_{RO} = \dot{m}_{fuel} M_{O,stoi}$, where \dot{m}_{fuel} is the fuel mass flux and $M_{O,stoi}$ is the stoichiometric oxygen needed per kg of fuel.

Based on the above, the minimum required circulation can be calculated from (24) as:

$$\dot{m}_{s,in,min} = \frac{\dot{m}_{fuel} M_{O,stoi}}{R_{ox}} = 0.0227 \text{ kgs}^{-1}, \quad (25)$$

Keep in mind that the circulation calculated from Eq. (25) is the least acceptable recirculation amount for the specific fuel mass flux. In case we use less recirculation, it is sure that we will have unburnt fuel in the outlet. In practice, the needed circulation amount would be more, since at the output of the reactor the material is not completely reduced because of the fact that some of the reduction reactions are slow and also the mixing is not perfect in the reactor. Therefore, in this work, we selected the minimum recirculation value from the practically meaningful range. This way, this calculation will give an upper limit on the unburnt fuel. So, here one case is simulated for the minimum amount of circulation and another one with its double to investigate how this changes the results. The boundary conditions applied at the inlets and outlets are summarized in Table 8.

Table 8. Boundary conditions applied for the 10 kW_{th} case.

Boundary patch	Boundary condition	
	Gas/Solid	Flux
Distributor	Steam	26g/min
Fuel inlet	N ₂	5 L _n min ⁻¹
	Fuel particles	1.931 kgh ⁻¹
OC inlet	N ₂	5 L _n min ⁻¹
	OC flux	100% $\dot{m}_{s,in,min}$, 200% $\dot{m}_{s,in,min}$ where $\dot{m}_{s,in,min}$ is based on Eq. (25)
OC outlet	N ₂	Calculated from the CFD simulation considering a gauge pressure of 10 Pa
	OC flux	Calculated from CFD
Flue gas outlet	Gauge pressure = 0	

2.3.1.2. Cases considered

The simulated cases for the 10 kW_{th} reactor are summarized in Table 9. Two base cases without packings were considered:

- One with the minimum required circulation (as calculated from Eq. (25))
- One with double the minimum circulation to investigate its effect

In addition, a third case was simulated using the same higher circulation rate but with packings installed in the reaction zone. The packings extend up to the oxygen carrier outlet, following suggestions from the project partners at CTH. They are modelled using a non-uniform porosity field, shown in Figure 14, to better approximate the hydrodynamic effects introduced by the packing elements.

Table 9. Simulated cases for the 10 kW_{th} reactor at CTH

Case ID	Circulation flux (kgh ⁻¹)	Packings
LowCirc	81.72	No
HighCirc	163.44	No
HighCircPack	163.44	Yes

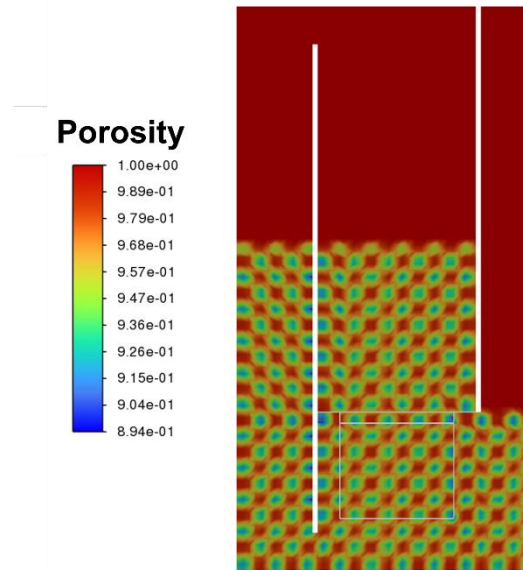


Figure 14. Non-uniform porosity field applied.

2.3.2. Spanish National Research Council (CSIC) 20 kW_{th} pilot plant

A schematic representation of the 20 kW_{th} CLC pilot plant at CSIC is shown in Figure 15. The fuel reactor is a cylindrical circulating bed reactor. The figure also indicates the various inlets and outlets of the reactor.

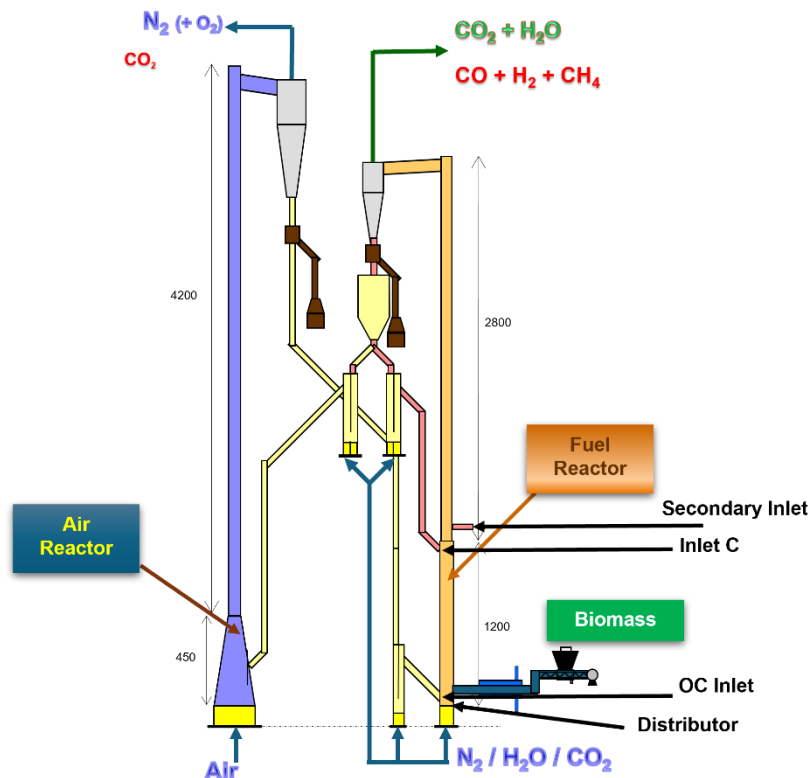


Figure 15. Schematic representation of the 20 kW_{th} CLC unit at CSIC.

The fluidization gas, consisting of 100% CO₂, is introduced mainly through the distributor inlet located at the bottom of the reactor. However, a portion of this gas can optionally be redirected through a secondary inlet. This strategy is used to enhance the solid inventory and increase the residence time of solids in the dense region of the reactor, thereby improving reaction conditions. The loop seals in the system are fluidized with nitrogen (N₂).

The geometry used for CFD simulations is shown in Figure 16 (a). The corresponding mesh, created using ANSYS Fluent Meshing, consists of approximately 15500 polyhedral cells and is shown in Figure 16 (b).

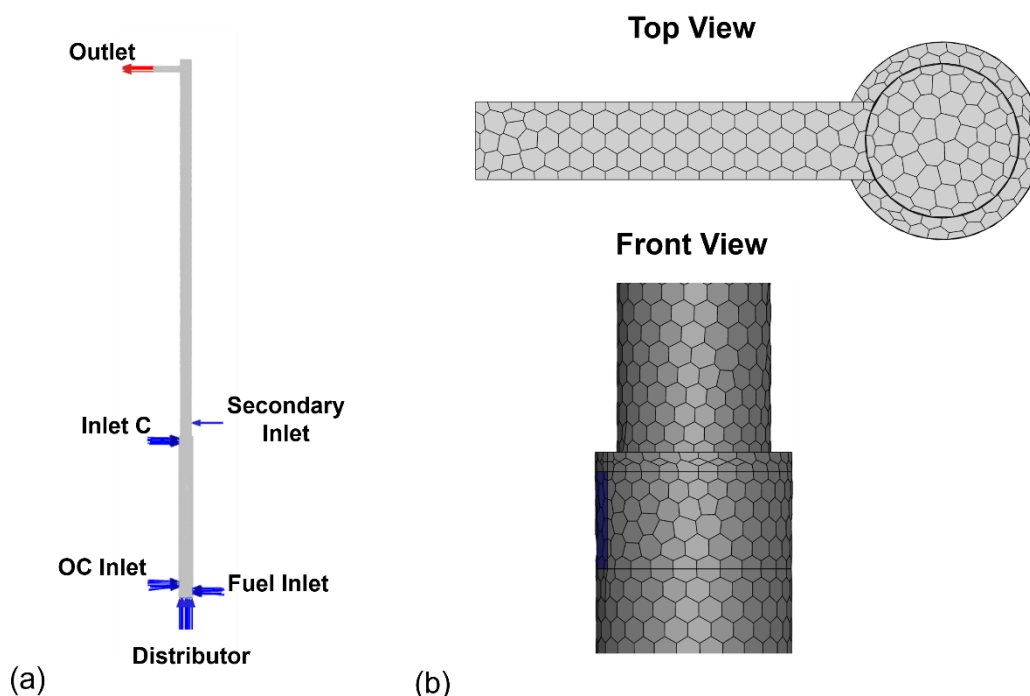


Figure 16. CAD geometry used in the simulations (a), and (b) top and front view of the computational grid.

2.3.2.1. Boundary and operating conditions

Isothermal simulations are applied, and the temperature was set at 900 °C. Since the actual experiments at CSIC had not yet started at the time of the simulations, only estimated values were available for both the inventory (3kg-6kg) and circulation flux (~200 kg/h). Therefore, the circulation flux is 126% of the minimum required flux as calculated from Eq. (25). Two modelling approaches were adopted regarding the circulation of the oxygen carrier (OC). In the first approach, a fixed OC circulation flux of 200 kg/h was imposed, allowing the bed inventory to develop naturally during the simulation. In the second approach, the OC inventory was fixed at 6 kg, which is at the upper end of the 3–6 kg range estimated by the experimental partners. In this case, the OC exiting the reactor was fully recycled back to the OC inlet, under the assumption that it enters the fuel reactor in a fully oxidized state (i.e., after passing through the air reactor).

The fuel reactor operates with CO₂ as the fluidization gas. A total of 9000 L_nh⁻¹ of CO₂ is injected into the reactor, of which 6000 L_nh⁻¹ is introduced through the bottom distributor and 3000 L_nh⁻¹ through the secondary inlet. However, the precise gas distribution between these two inlets remains to be validated during the experiments. Additional gas is supplied at the following locations: 1000 L_nh⁻¹ CO₂ through the screw feeder (together with the solid fuel), 500 L_nh⁻¹ N₂ through the OC inlet, and 500 L_nh⁻¹ N₂ through Inlet C, bringing the total gas input to 11000 L_nh⁻¹.

The fuel feed is set to 4 kg/h of biomass, corresponding to a thermal input of 20 kW_{th}. It is noted that the fluidization behavior of the reactor is influenced not only by the externally injected gases but also by gases released during fuel conversion processes (drying, devolatilization, and gasification).

During the simulation of the fixed inventory case, it was observed that the initially assigned primary gas flow (through the distributor only) was insufficient to properly fluidize the biomass particles. To ensure stable fluidization and circulation, the secondary gas stream was redirected to enter through the distributor. The boundary conditions are summarized in Table 10.

Table 10. Boundary conditions for the 20 kW_{th} CSIC fuel reactor simulations.

Boundary patch	Boundary condition	
	Gas/Solid	Flux
Distributor	CO ₂	6000 - 9000 L _n h ⁻¹
Fuel inlet	CO ₂	1000 L _n h ⁻¹
	Fuel particles	4 kg h ⁻¹
OC inlet	N ₂	500 L _n h ⁻¹
	Fully oxidized OC	Fixed at 200 kg h ⁻¹ or recirculated
Inlet C	N ₂	500 L _n h ⁻¹
Secondary Inlet	CO ₂	0 – 3000 L _n h ⁻¹
Outlet	Gauge pressure = 0	

2.3.2.2. Simulated cases

Two simulation scenarios were examined:

1. Fixed Circulation: OC flux set to 200 kg/h.
2. Fixed Inventory: Inventory set to 6 kg; circulation allowed to develop from simulation. During the simulation, it was found that the initially defined primary gas flow was insufficient to fluidize the fuel particles. To address this, the secondary gas stream was redirected to the distributor to ensure proper fluidization and stable circulation.

The simulated cases are summarized in Table 11.

Table 11. Simulated cases for the 20 kW_{th} fuel reactor at CSIC.

Case ID	Circulation Strategy	OC Circulation (kg/h)	OC Inventory (kg)	Notes
CSIC-FC	Fixed circulation	200	Computed	Nominal primary/secondary gas split
CSIC-FI	Fixed inventory	Computed	6	Secondary gas redirected to distributor

2.3.3. Technical University of Darmstadt (TUDA) 1 MW_{th} pilot plant

CERTH received the mechanical drawings of the reactor from TUDA. Figure 17 (a) presents the geometry used in the CFD simulations. To facilitate mesh generation, all circular and elliptical inlet and outlet ducts were simplified to rectangular cross-sections. As shown in the figure, the reactor has a total length of approximately 11 m and an internal diameter of 400 mm. The bottom part of the reactor features a conical section, with the smallest diameter—280 mm—located at the distributor inlet. The various inlets and outlets are also labeled in the same figure. The computational grid was generated using ANSYS Fluent Meshing

and consists of approximately 76000 polyhedral cells. A close-up view of the bottom section of the mesh is shown in Figure 17 (b).

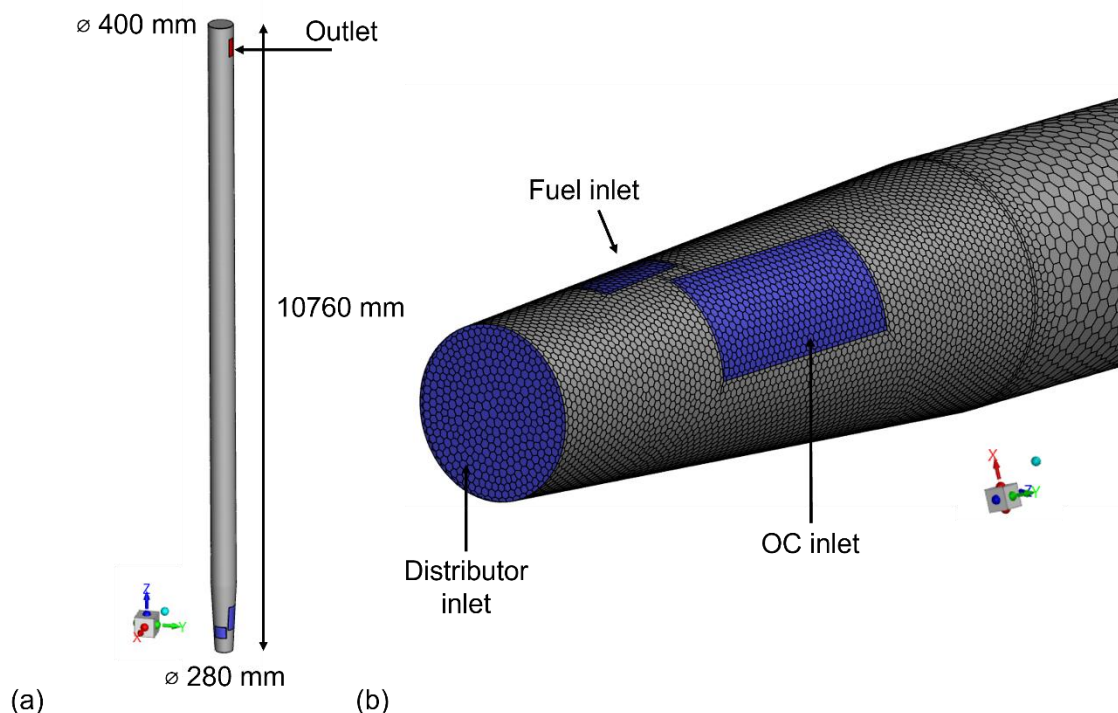


Figure 17. (a) CAD geometry of the 1 MW_{th} fuel reactor at TUDA and (b) close-up view of the computational grid in the bottom section of the reactor.

2.3.3.1. Boundary and operating conditions

The CFD setup for the TUDA 1 MW_{th} fuel reactor is based on preliminary information provided by the project partners. Recycled flue gas enters the reactor through the distributor at a rate of 527.5 Nm³h⁻¹, corresponding to an estimated fluidization velocity of approximately 5 m/s. The assumed composition of this gas is shown in Table 12.

Fuel is introduced through the fuel inlet at a mass flow rate of 195.55 kg h⁻¹, along with 10 Nm³h⁻¹ of CO₂. An additional 10 Nm³h⁻¹ of CO₂ is introduced via the oxygen carrier (OC) inlet. The total solid inventory is estimated in the range of 60–85 kg, while the circulation flux is given as 13,446 kg h⁻¹, corresponding to 185% of the minimum required value (from Eq. (25).). These values are approximations and may be revised based on future experimental results.

Based on insights gained from the CSIC case, where inventory was shown to significantly impact conversion, the simulation strategy here was to fix the inventory at its upper estimated value (85 kg) and recirculate all oxygen carrier exiting the reactor, assuming it re-enters in a fully oxidized state after passing through the air reactor.

Table 12. FR inlet gas composition assumed for wood-pellets fuel.

Species	Composition (wt-%)
CO ₂	43.17%
H ₂ O	54.21%
O ₂	2.33%
NO ₂	0.27%
SO ₂	0.02%

Table 13. Boundary conditions for the 1 MW_{th} TUDA fuel reactor simulations.

Boundary patch	Boundary condition	
	Gas/Solid	Flux/Value
Distributor	Recycled flue gas – Assumed composition is given in Table 12	527.5 Nm ³ h ⁻¹
Fuel inlet	CO ₂	10 Nm ³ h ⁻¹
	Fuel particles	195.55 kg h ⁻¹
OC inlet	CO ₂	10 Nm ³ h ⁻¹
	Fully oxidized OC	Recirculated/Calculated from simulation
Outlet	Gauge pressure = 0	

2.3.3.2. Simulated cases

Two cases were simulated to examine the impact of solid inventory on fuel conversion. The first used an inventory of 85 kg, based on the maximum expected value provided by TUDA. Since this case resulted in low conversion, a second case was simulated with a roughly doubled inventory of 160 kg. The simulated cases are summarized in Table 14.

Table 14. Simulated cases for the 1 MW_{th} TUDA fuel reactor.

Case ID	Inventory (kg)
TUDA-85	85
TUDA-160	160

3. CFD MODELLING RESULTS

3.1. CFD modelling of the fuel reactor of CTH 10 kW_{th} pilot plant

CFD simulations of the 10 kW_{th} fuel reactor were computationally intensive. Due to the stiff nature of the problem at hand (i.e., multiphase flow with two Eulerian phases describing the continuous gas-phase and the dense OC particles and one Lagrangian phase describing the fuel particles, including both heterogeneous and homogeneous reactions), a relatively low time-step equal to 2.e-4 is required to ensure numerical stability. Each simulation was run for at least 150s of physical time, resulting in a minimum of 750000 time-steps per case. Once a quasi-steady state was reached, results were time-averaged over a 50-second window.

Given that the three simulated cases (“**LowCirc**”, “**HighCirc**”, “**HighCircPack**” — see Table 9) exhibited broadly similar flow and species distribution patterns, the following analysis focuses primarily on the “**HighCirc**” case. For the other cases, only key differences will be discussed.

Flow and Mixing Patterns

Figure 18 shows the instantaneous solid volume fraction (VOF) contour at a vertical mid-plane of the reactor for the HighCirc case. Large bubbles are observed forming at the top of the volatile distributor (VD), expanding as height increases. This behaviour is attributed to the additional gases generated by fuel moisture and devolatilization, which are injected at high velocity through the VD’s narrow opening. Additionally, the bed surface level adjacent to the VD is noticeably lower than in the central region. This results from increased gas pressure due to the volatiles being forced through the distributor’s restricted exit. The accumulated gas raises the local pressure, which in turn suspends the bed material, lowering the apparent bed level outside the VD.

Figure 19 presents the corresponding solid volume fraction contour for the “**HighCircPack**” case. Visually, no significant difference in bubble patterns or bed structure is observed compared to the “**HighCirc**” case, suggesting that under current conditions, the packings have limited influence on hydrodynamics.

To further illustrate flow behaviour around the VD, Figure 20 presents velocity magnitude contours on both the mid-plane and a cross-sectional slice normal to the z-axis intersecting the VD opening. A significant velocity increase is observed as volatiles exit the volatile distributor, confirming the intense gas injection into the dense bed. Figure 21 overlays velocity vectors on a CH₄ mass fraction contour at the mid-plane. It is evident that CH₄ enters the bed through the VD and disperses rapidly within the bed region, where it is subsequently consumed by heterogeneous reduction reactions with the OC particles.

Figure 22 shows instantaneous contours of the combustible volatiles (CH₄, CO, H₂). These gases are produced in the downer duct, quickly after the solid fuel particles are injected from the top of the reactor downwards. Then, these gases are transported through the VD in the main bed area, where they are quickly consumed by heterogeneous reactions with the OC particles. Figure 23 shows the H₂O and CO₂ species instantaneous contours at time 100s. H₂O, used as the fluidization medium, is initially dominant at the bottom area of the bed, but becomes diluted by CO₂, which is produced from fuel conversion, as height increases. Additionally, some H₂O is released from fuel moisture and devolatilization processes. From the same figure, it can also be observed that CO₂ is primarily produced in the main section of the reactor (through the VD region) and exits mainly through the gas outlet. A fraction of it, however, crosses the left middle wall and is directed toward the OC outlet.

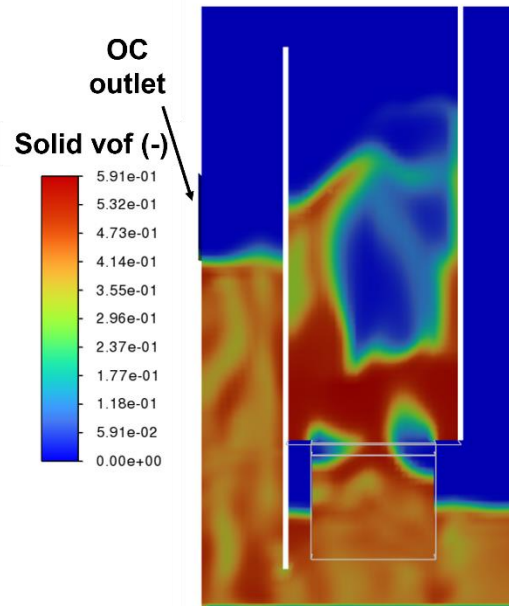


Figure 18. Mid-plane vof contour for the HighCirc case.

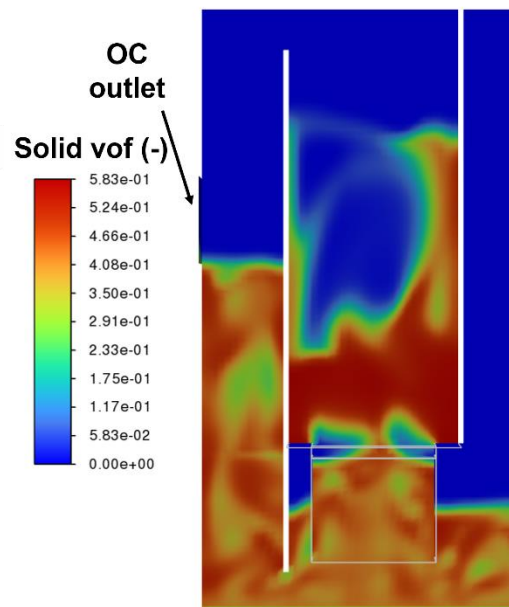


Figure 19. Mid-plane vof contour for the HighCircPack case.

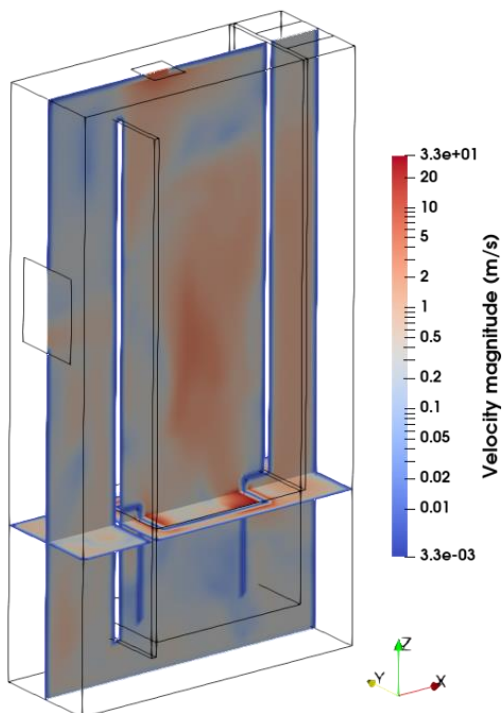


Figure 20. Velocity magnitude (log scale) contours at the mid-plane and at a cross-section normal to the z-axis, intersecting the volatile distributor opening.

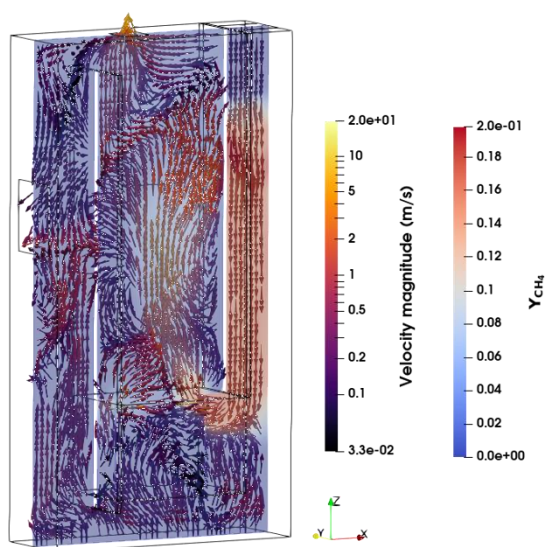


Figure 21. Velocity vectors on the mid-plane, colored by velocity magnitude (log scale), overlaid on a CH_4 concentration contour.

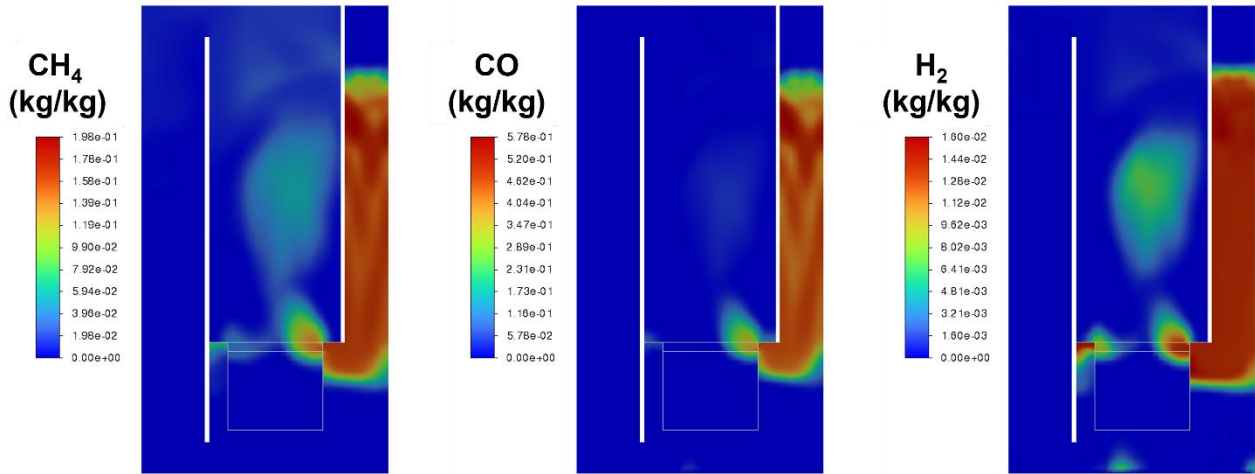


Figure 22. Mid-plane combustible volatile species contours for the HighCirc case at $t = 100s$.

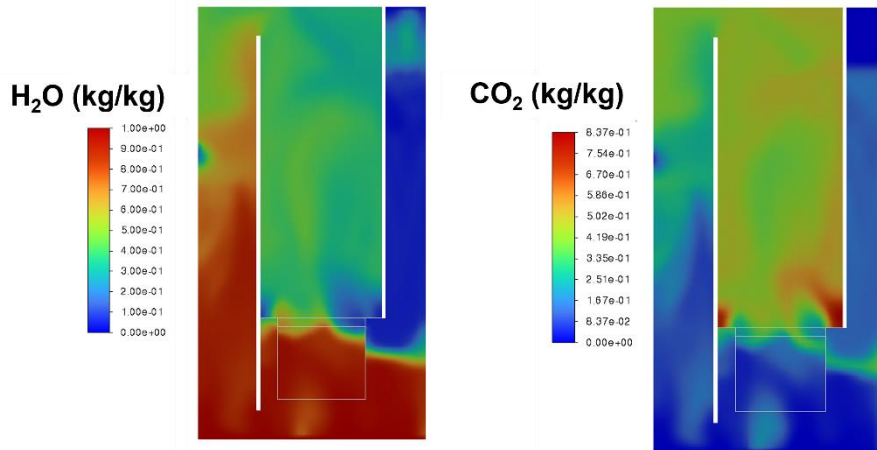


Figure 23. Mid-plane H_2O and CO_2 species contours for the HighCirc case at $t = 100s$.

Outlet gas compositions

Figure 24 shows the time evolution of the area-weighted average of species mass fractions at the flue gas outlet, during the averaging period, for the HighCirc case. Although all species exhibit fluctuations, their average values remain stable over time, indicating that a quasi-steady state has been achieved. The mean outlet compositions for all cases are summarized in Table 15.

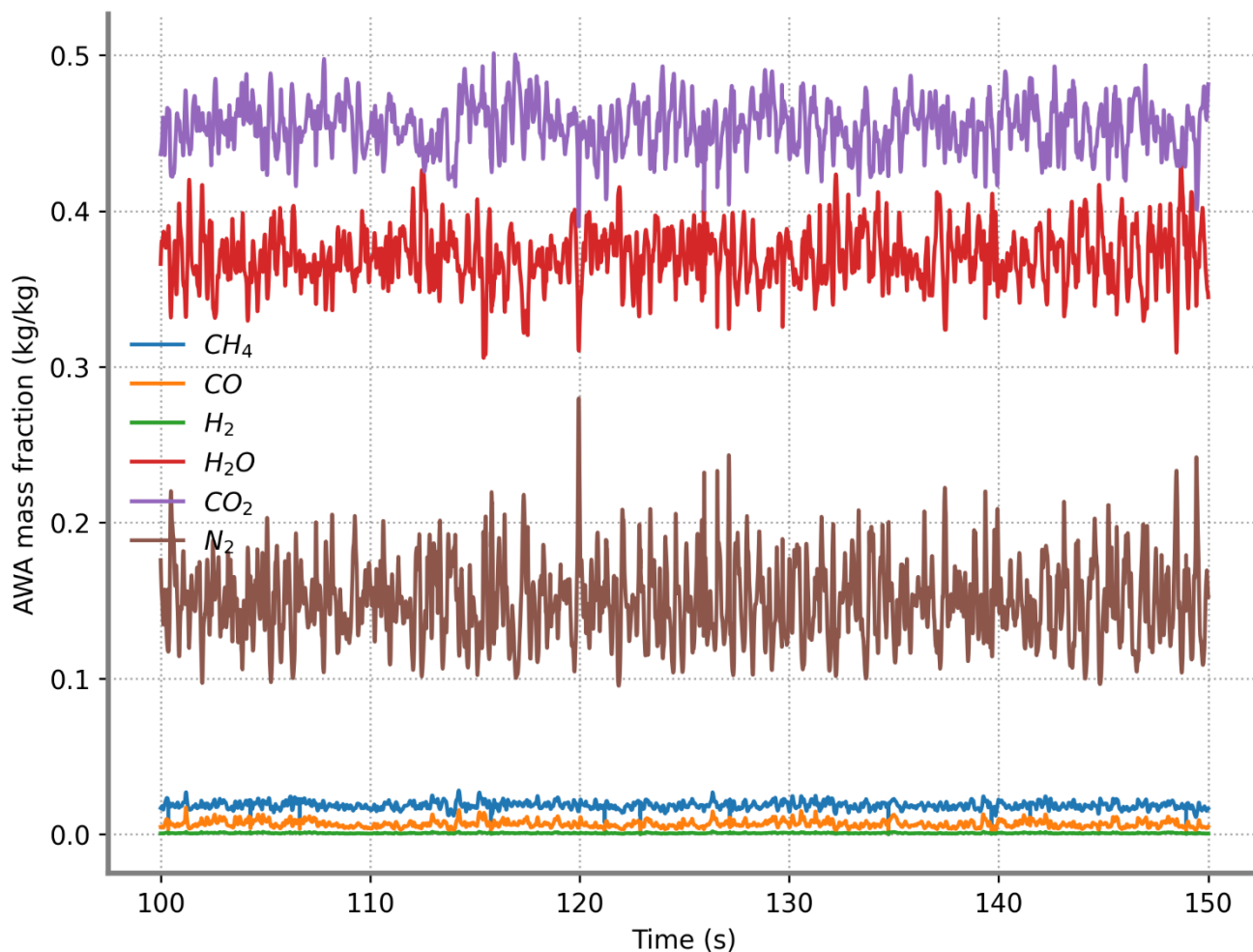


Figure 24. Area-weighted averaged species mass fractions at the reactor outlet (HighCirc case).

Table 15. Average outlet gas-phase species mass fractions (kg/kg %) for the three simulated cases.

Species	LowCirc	HighCirc	HighCircPack
CO ₂	44.53	45.43	45.3
H ₂ O	37.08	37.06	36.98
CH ₄	2.23	1.86	1.97
CO	0.97	0.66	0.7
H ₂	0.11	0.07	0.08
O ₂	0	0	0
N ₂	15.08	14.92	14.97

Particle Residence Time Distribution

Figure 25 indicatively shows the fuel particle positions for the HighCirc case at $t = 100$ s. In this figure, the particles are colored by their residence time. Particles near the fuel inlet exhibit lower residence times. Then, they are carried to the main bed area, where they recirculate, increasing their residence time.

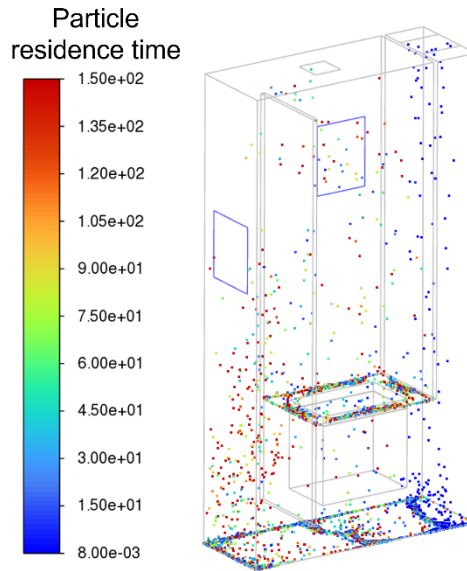


Figure 25. Particle positions inside the domain at $t = 150$ s coloured by the residence time.

Integral Performance Metrics

Table 16 summarizes key performance metrics for the simulated cases, including inventory, residence times, OC conversion, char gasification, and O_2 -based efficiency. The average OC residence time is calculated as follows:

$$t_{OC} = \frac{Inventory}{\dot{m}_{OC}} \quad (26)$$

The O_2 -based efficiency is calculated by comparing the stoichiometric oxygen needed to **completely** convert the fuel ($O_{fuel,stoi}$) with the stoichiometric oxygen required to convert the combustible gases ($O_{flue-gas,stoi}$) and the exiting char particles at the reactor's outlet, i.e.:

$$O_{eff} = 1 - \frac{O_{flue-gas,stoi}}{O_{fuel,stoi}} \quad (27)$$

The solids inventory remained constant across all cases (~ 4.9 kg), as expected. In bubbling beds, bed height and solids inventory are primarily governed by fluidization parameters and reactor geometry (e.g. the placement of OC outlet) rather than circulation flux. The high porosity of packings also has a negligible impact on the overall inventory.

The average OC residence time was 108 s in the “**HighCirc**” case, doubling to 216 s in the “**LowCirc**” case. Accordingly, the average OC conversion decreased from 54% (“**LowCirc**”) to 32% (“**HighCirc**”) as increased circulation renews the bed material more frequently, resulting in less converted OC in the inventory.

Regarding the O₂-based efficiency, it was slightly higher at the “**HighCirc**” (73%) case than the “**LowCirc**” case (71.7%). However, the increase is slight (73% vs 71.7%). This modest improvement indicates that higher circulation improves the burnout of volatiles. However, the gain is limited. To understand why, the percentage of gasified char was examined. It was observed that the “**LowCirc**” case achieved a higher char gasification percentage. This is attributed to the increased fuel residence time (66s in “**LowCirc**” versus 40s in the “**HighCirc**” case), which allows char particles more time to undergo gasification reactions. The reason for the reduced fuel residence time in “**HighCirc**” is that increased circulation drags more the fuel particles toward the OC outlet, leading to premature exit from the reactor. However, this negative effect on char conversion is overcompensated by the better mixing and faster oxidation of volatiles in “**HighCirc**” case, which results in higher volatile burnout efficiency, and, eventually, lower concentrations of unburnt gases at the reactor outlet. This can be clearly seen in Table 15, where “**LowCirc**” exhibits higher outlet mass fractions of combustible gases (CH₄, CO, H₂).

Table 16. Integral Performance Metrics for CTH Cases.

Case ID	Inventory (kg)	Avg. OC Residence Time (s)	Avg. OC Conversion (%)	Avg. Fuel Residence Time (s)	Char Gasified (%)	O ₂ -Based Efficiency (%)
LowCirc	4.9	216	54	66	72.5	71.7
HighCirc	4.9	108	32	40	66	73
HighCircPack	4.9	108	32	45	66.8	73

Another noteworthy observation is that a considerable amount of unconverted fuel char particles leaves the domain through the OC outlet. This is unwanted, since these particles will later burn in the air reactor, reducing the CO₂ capture efficiency of the pilot plant. In particular, in the “**LowCirc**” case, 54.61 % of the char leaving the reactor leaves through the OC outlet, while this percentage increases to 69.54% in the “**HighCirc**” case. This shows that the higher circulation of OC particles indeed drags more fuel particles to leave the reactor, thus decreasing their residence time.

Effect of Packings (HighCircPack Case)

The inclusion of packings in the “**HighCircPack**” case did not significantly impact O₂-based efficiency compared to “**HighCirc**” (73%). However, a slight increase in fuel residence time (+5 seconds) and char gasification (from 66% to 66.8%) was observed. This can be attributed to the additional drag imposed by the packings to the fuel particles, which delay their exit from the reactor.

A visual comparison of hydrodynamics (Figure 18 versus Figure 19) revealed minimal differences in bubble sizes between cases with and without packings. This limited impact is attributed to the strong fluidization already induced by the volatile distributor, which dominates the flow dynamics in the central region of the bed. To quantify this observation, Table 17 reports the average bubble fraction and bed voidage for both cases. Applying the correlations of Eqs. (19)-(23), these values translate into negligible differences in the estimated bubble sizes.

In summary, under the current reactor configuration, the packings appear to have a limited influence on bed hydrodynamics. However, it is anticipated that the slight increase in fuel residence time could help reduce the amount of unconverted char leaving through the OC outlet. Experimental validation is recommended to confirm these observations, particularly regarding potential reductions in unburnt char at the reactor outlet.

Table 17. Average bubble fraction and voidage for the high circulation simulations with and without packings.

Case ID	δ	ϵ_f
---------	----------	--------------

HighCirc	0.1765	0.6032
HighCircPack	0.1771	0.60299

3.2. CFD modelling of the fuel reactor of CSIC 20 kW_{th} pilot plant

CFD simulations of the 20 kW_{th} fuel reactor were computationally intensive. Similar to the CTH 10 kW_{th} reactor, due to the stiff nature of the problem at hand, a small time-step of 2.e-4 s was required for numerical stability. Time-averaged quantities were calculated over a 50-second interval after the establishment of a quasi-steady state.

Figure 26 shows the solid volume fraction contours on the reactor's mid-plane normal to the y-axis for "CSIC-FC" and "CSIC-FI". The "CSIC-FC" case stabilizes at a much lower inventory (~1.5 kg) compared to the 6 kg imposed in "CSIC-FI", which is clearly reflected in the volume fraction contours.

Figure 27 - Figure 31 present the gas species mass fraction contours (CH₄, CO, H₂, H₂O, CO₂) on the same mid-plane. In both cases, combustible species (CH₄, CO, H₂) are generated in the lower part of the reactor, near the fuel inlet, and gradually decrease in concentration with height as they are consumed in reduction reactions with OC particles. The "CSIC-FI" case exhibits faster consumption of these gases, attributed to the larger inventory of reactive OC particles enhancing conversion.

Regarding H₂O (Figure 30), formation starts at the bottom, due to biomass drying, but the majority result from heterogeneous OC reduction. In the "CSIC-FC" case, H₂O concentration initially rises, drops slightly around the secondary CO₂ inlet (due to dilution), and increases again as OC particles continue to react higher in the bed. The CO₂ field (Figure 31) is dominated by two sources: the injected CO₂ (fluidization medium) and the heterogeneous reduction reaction products. As a result, CO₂ is the most abundant gas in both cases.

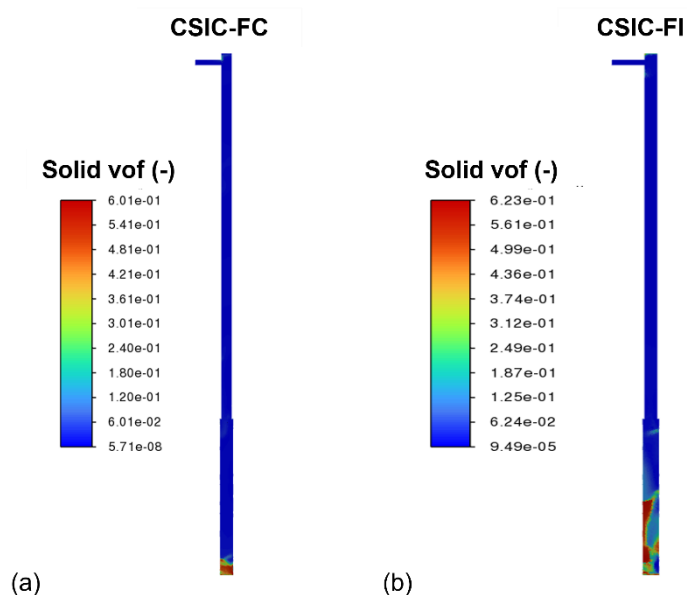


Figure 26. Solid-VOF contour on a mid-plane normal to the y-axis for cases CSIC-FC (a) and CSIC-FI (b).

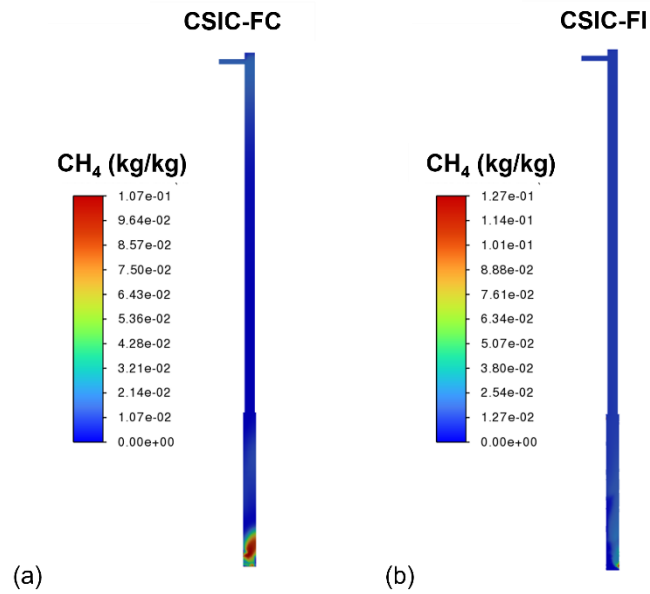


Figure 27. CH₄ mass fraction contour on a mid-plane normal to the y-axis for cases CSIC-FC (a) and CSIC-FI (b).

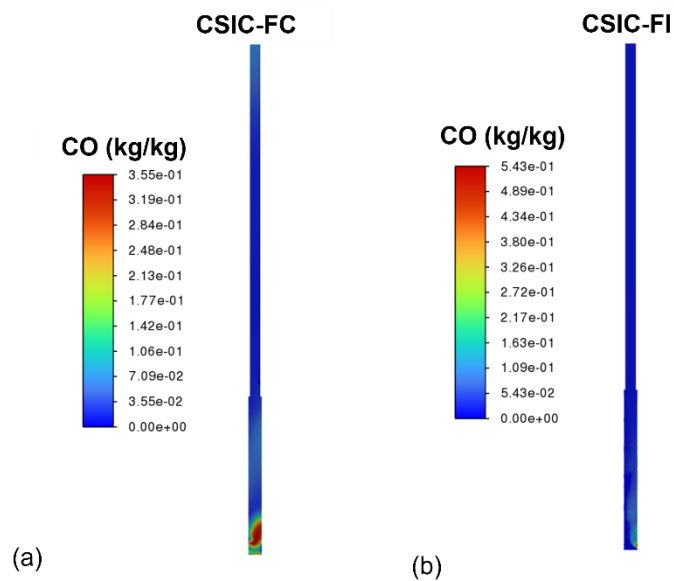


Figure 28. CO mass fraction contour on a mid-plane normal to the y-axis for cases CSIC-FC (a) and CSIC-FI (b).

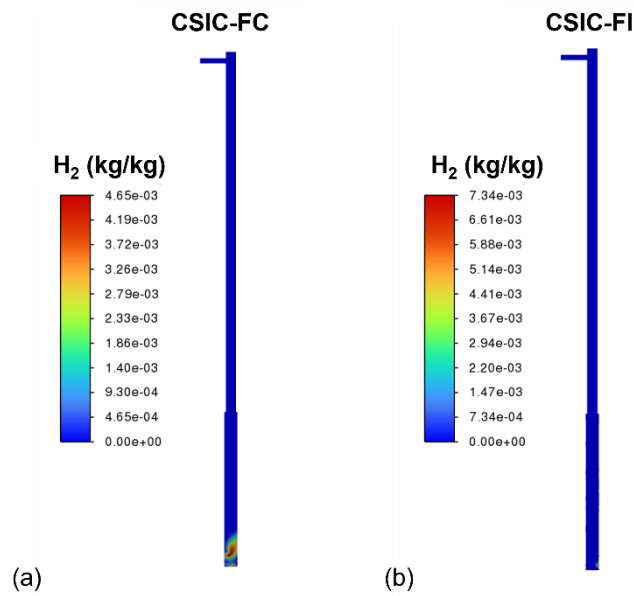


Figure 29. H₂ mass fraction contour on a mid-plane normal to the y-axis for cases CSIC-FC (a) and CSIC-FI (b).

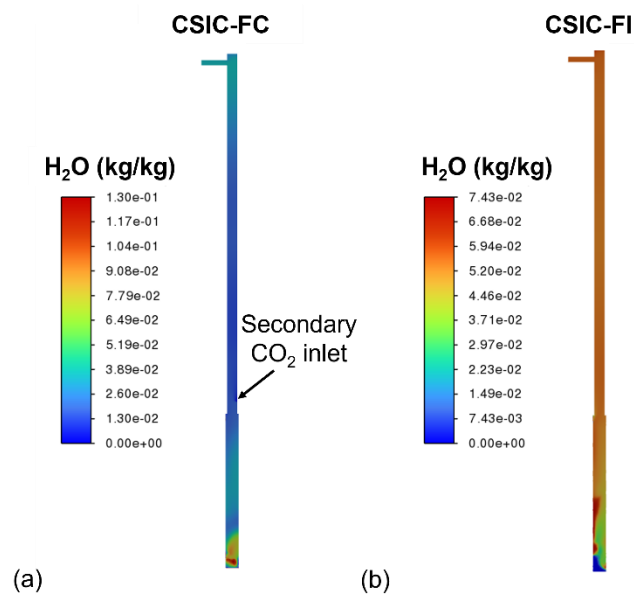


Figure 30. H₂O mass fraction contour on a mid-plane normal to the y-axis for cases CSIC-FC (a) and CSIC-FI (b).

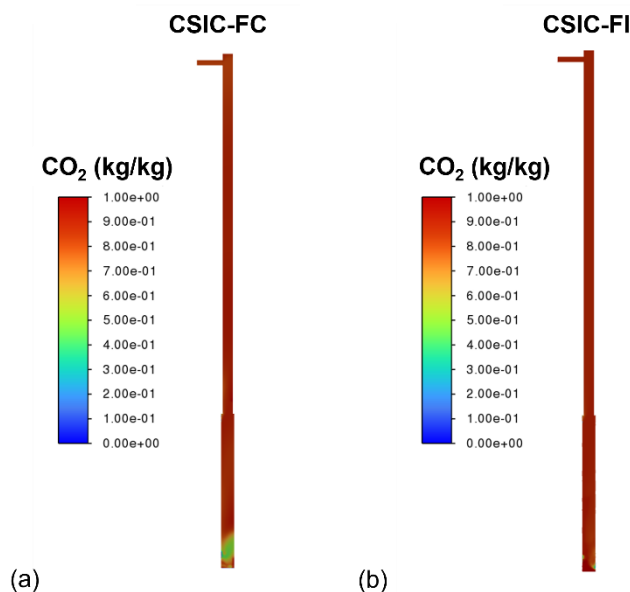


Figure 31. CO₂ mass fraction contour on a mid-plane normal to the y-axis for cases CSIC-FC (a) and CSIC-FI (b).

Table 18 reports the outlet gas-phase species mass fractions for the CSIC cases. CO₂ concentrations exceed 80% in both cases—82% in "**CSIC-FC**" and 88.9% in "**CSIC-FI**". The concentrations of combustible gases at the outlet are lower in "**CSIC-FI**", confirming improved fuel conversion. This is attributed to the higher inventory, which increases the probability of interactions between fuel-derived gases and reactive OC particles.

Table 18. Average outlet gas-phase species mass fractions (kg/kg %) for the CSIC cases.

Species	CSIC-FC	CSIC-FI
CO ₂	82	88.9
H ₂ O	4	5.7
CH ₄	1.7	1.2
CO	6.5	1.9
H ₂	0	0
O ₂	0	0
N ₂	5.6	2.1

Table 19 presents the integral performance metrics for the CSIC cases. The fixed inventory case ("**CSIC-FI**") operated with nearly four times more solids than "**CSIC-FC**". This had a strong effect on fuel conversion efficiency, as measured by the O₂-based efficiency metric (see Eq. (27)). In particular, "**CSIC-FI**" achieved 43% efficiency, whereas "**CSIC-FC**" reached only 16%. The large improvement is attributed to the higher likelihood of oxidizing combustible gases before they exit the reactor, thanks to the denser regime of "**CSIC-FI**".

Table 19. Integral Performance Metrics for CSIC Cases.

Case ID	Inventory (kg)	Circulation (kg/h)	Avg. OC Residence Time (s)	Avg. OC Conversion (%)	Char Gasified (%)	O ₂ -Based Efficiency (%)
CSIC-FC	1.58	200	28	20	72	16
CSIC-FI	6	1070	20	11.7	72	43

3.3. CFD modelling of the fuel reactor of TUDA 1 MW_{th} pilot plant

The time step applied for the simulations was $2 \cdot 10^{-4}$ s. The time-averaged quantities are calculated for a time-period of 20 s after the achievement of a quasi-steady state. For this reactor, two cases were considered, differing in inventory: "**TUDA-85**" (85 kg) and "**TUDA-160**" (160 kg).

Figure 32 shows the solid volume fraction contours on a mid-plane normal to the y-axis. The higher inventory in "**TUDA-160**" leads to a visibly denser bed behaviour compared to "**TUDA-85**". However, flow patterns in most of the reactor domain are dilute. This is expected, as the reactor operates in the circulating fluidized bed regime.

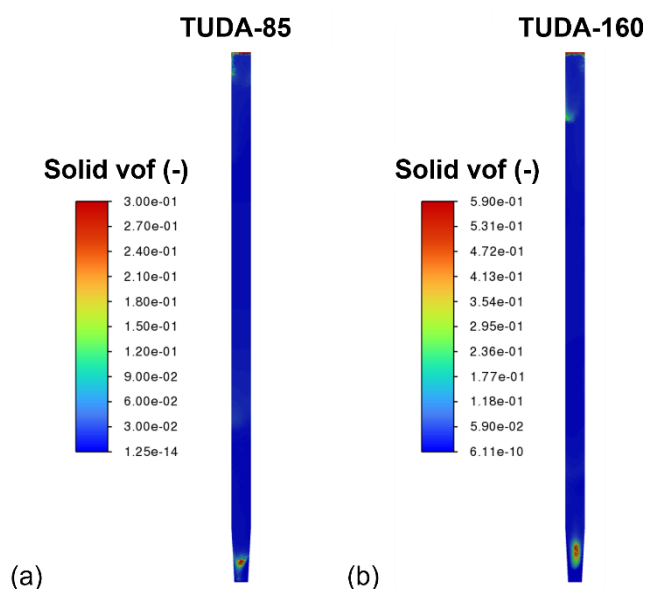


Figure 32. Solid-VOF contour on a mid-plane normal to the y-axis for cases TUDA-85(a) and TUDA-160 (b).

Figure 33 - Figure 37 present the contours of time-averaged CH_4 , CO , H_2 , H_2O , and CO_2 mass fractions. Combustible species (CH_4 , CO , H_2) are generated in the lower bed region and decrease in concentration with height, as they are consumed through heterogeneous reactions with the OC particles. As expected, "**TUDA-160**", having more OC available, results in lower concentrations of combustibles in the upper part of the bed. CO_2 and H_2O distributions confirm the enhanced conversion in this case, with more complete oxidation of fuel.

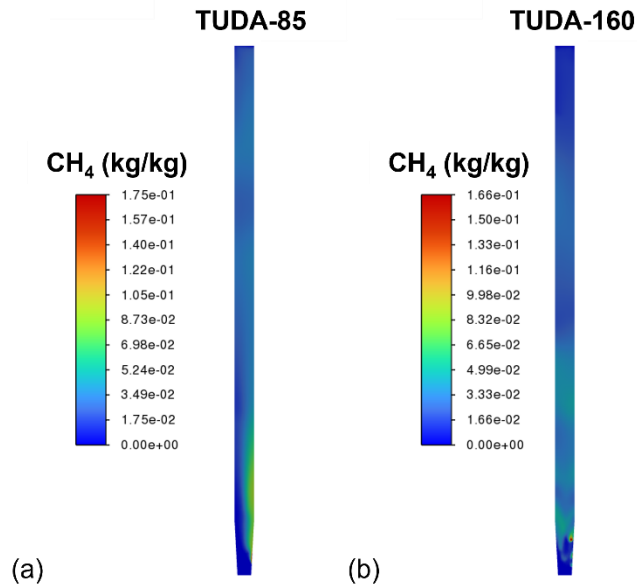


Figure 33. CH₄ mass fraction contour on a mid-plane normal to the y-axis for cases TUDA-85(a) and TUDA-160 (b).

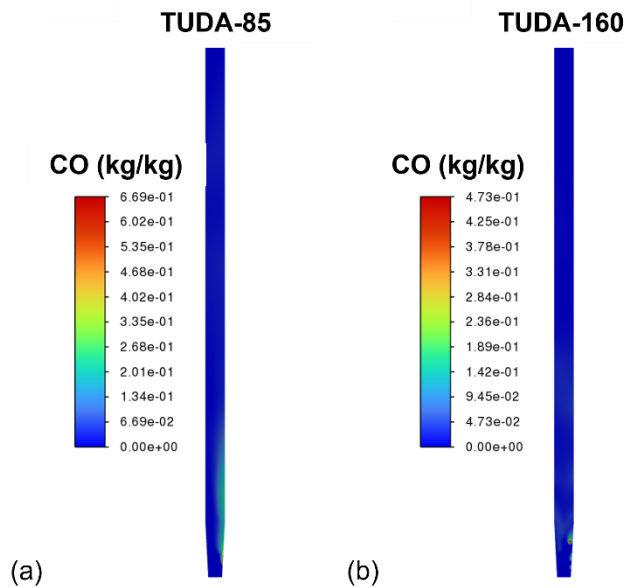


Figure 34. CO mass fraction contour on a mid-plane normal to the y-axis for cases TUDA-85(a) and TUDA-160 (b).

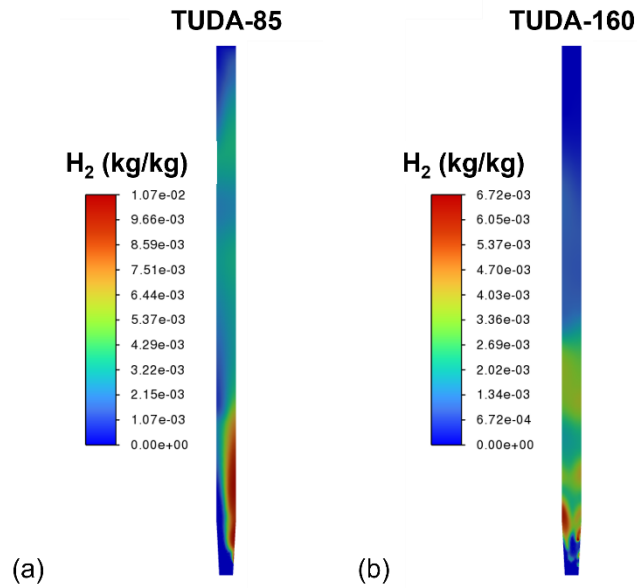


Figure 35. H₂ mass fraction contour on a mid-plane normal to the y-axis for cases TUDA-85(a) and TUDA-160 (b).

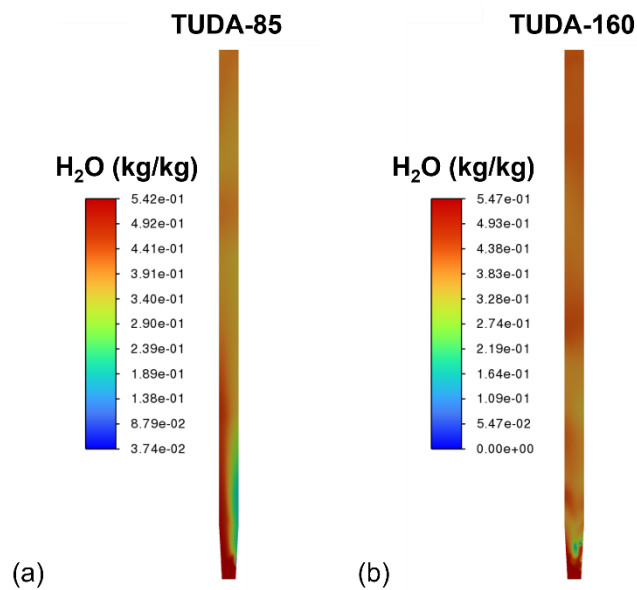


Figure 36. H₂O mass fraction contour on a mid-plane normal to the y-axis for cases TUDA-85(a) and TUDA-160 (b).

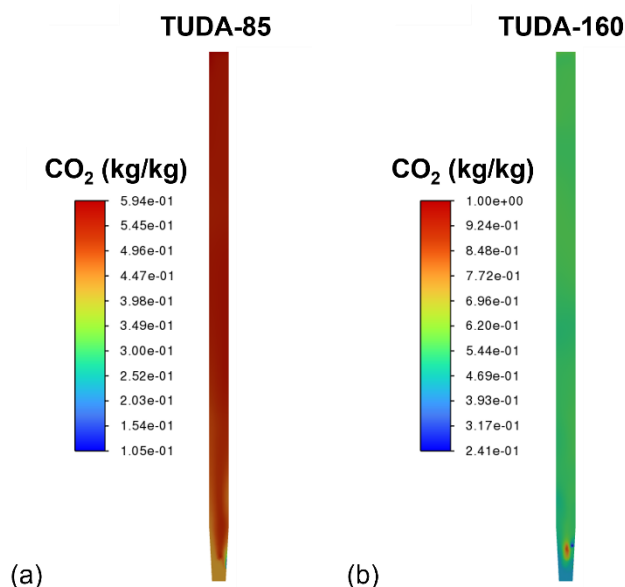


Figure 37. CO₂ mass fraction contour on a mid-plane normal to the y-axis for cases TUDA-85(a) and TUDA-160 (b).

Table 20 reports the time-averaged gas composition at the reactor outlet. "TUDA-160" exhibits lower concentrations of CH₄, CO, and H₂ compared to "TUDA-85", indicating more efficient fuel conversion. CO₂ and H₂O concentrations are also slightly higher, reflecting greater oxidation extent.

Table 20. Average outlet gas-phase species mass fractions (kg/kg %) for the TUDA cases.

Species	TUDA-85	TUDA-160
CO ₂	56	57
H ₂ O	41	41
CH ₄	2.7	1.70
CO	0.64	0.087
H ₂	0.084	0.011
O ₂	0	0
N ₂	0.27	0.26

Integral performance indicators are summarized in Table 21. The table shows a significant difference in O₂-based efficiency: "TUDA-160" achieves 71%, nearly four times higher than the 21% of "TUDA-85". This again highlights the importance of inventory in such reactors. As discussed previously for the CSIC reactor in Section 3.2, when the inventory is higher, there is a greater chance for the fuel combustible volatiles to meet an OC particle and convert to CO₂ and H₂O.

Table 21. Integral Performance Metrics for TUDA Cases.

Case ID	Inventory (kg)	Circulation (kg/h)	Avg. OC Residence Time (s)	Avg. OC Conversion (%)	Char Gasified (%)	O ₂ -Based Efficiency (%)
TUDA-85	85	150000	2	1	92	21
TUDA-160	160	202484	2.9	1	91	71

4. CONCLUSIONS

This report presented CFD simulations of the fuel reactors associated with the pilot plants of the project partners: the 10 kW_{th} fuel reactor of CTH, the 20 kW_{th} fuel reactor of CSIC, and the 1 MW_{th} fuel reactor of TUDA.

A key design feature explored in this work was the use of packings to enhance the mixing between oxygen carrier (OC) particles and the combustible gases released from biomass fuel. These packings have been extensively studied at CTH under bubbling fluidized bed conditions in a lab-scale batch reactor. To the best of the authors' knowledge, no prior CFD studies have modelled packings in fluidized reactors. Following the project proposal, packings were modelled using a porous medium approach, as resolving their actual geometry is computationally infeasible even at lab scale. The porous model was applied and evaluated using available experimental data from the CTH lab-scale reactor.

The simulations showed that a uniform porosity field failed to capture the influence of the packings on gas–solid flow. When a non-uniform porosity profile, based on trigonometric functions, was introduced, the model showed a clear impact on the average bubble size. However, the predicted improvement in conversion was lower than the experimental one (5% vs. 20%). This highlights a limitation of current porous media approaches in CFD when applied to packed fluidized beds for modelling the packings. Based on this result, the simulations for all three pilot reactors were initially carried out without packings, in line with the fact that all units will first be operated without packings and that this assumption provides a conservative (worst-case) scenario for performance evaluation. The CTH bubbling fluidized bed reactor was later used to further investigate the effect of packings, due to its similarity to the lab-scale experimental unit (since it is a bubbling bed reactor).

Regarding the CTH 10 kW_{th} fuel reactor simulations, the results showed that under the supplied operating conditions, the expected O₂-based efficiency is approximately 70%. Increasing the circulation rate slightly improved efficiency, mainly because volatile gases were converted more effectively. However, the increased circulation increased the unburnt char exiting the reactor from the OC outlet. This trade-off, as well as the overall results of the studied computational cases suggest that the limiting factor is not the supply of fully oxidized oxygen carrier, but the residence time of fuel particles and volatiles. Since this reactor operates in a bubbling fluidized bed regime, increasing the inventory is not straightforward, as it is primarily governed by the position of the OC outlet and the fluidization gas flux. Therefore, a slight reduction in the fluidization flux may be a feasible strategy to improve fuel conversion. Regarding the inclusion of packings, the simulations showed no significant change in bubble size, likely due to the strong acceleration of gas flow through the small openings of the volatile distributor. However, packings were found to increase fuel particle residence time, leading to enhanced char gasification. These results are promising but should be experimentally validated, given the limitations of the porous media approach used to model the packings.

Regarding the CSIC 20 kW_{th} fuel reactor, the simulations clearly highlighted the critical role of solids inventory in achieving satisfactory fuel conversion. Even at the maximum provided value of 6 kg, the overall fuel conversion remained moderate (43%). This suggests that a higher inventory may be necessary to improve performance. Additionally, the default gas distribution strategy — with a significant portion (33%) of the main fluidization gas introduced through the secondary inlet — couldn't provide stable fluidization. This could be due to the relatively high position of the secondary inlet. A more effective strategy may involve supplying a larger fraction of the total gas flow from the bottom of the reactor.

For the TUDA 1 MW_{th} reactor, results showed that a fuel conversion of 71% can be achieved when an inventory of 160 kg is used — nearly double the maximum value in the initially supplied inventory range. Based on the volume fraction contours, there is room to further increase the inventory, which could potentially lead to even higher efficiencies.

It must be emphasized that the results presented here were obtained prior to the experiments. In practice, the actual experimental conditions may deviate from the assumptions used in the simulations. Moreover, several parameters — particularly the reaction kinetics — remain uncertain, as they are highly dependent on the specific oxygen carrier and fuel materials used. In addition, to stay on the conservative side, simulations were performed using the upper bound of fuel input (based on the nominal thermal power of each reactor). Lowering the fuel input would likely result in higher conversion values. Nevertheless, these limitations do not diminish the value of the findings. The simulations provide important qualitative insights that can guide experimental design and operation. Ultimately, it is anticipated that at least some of the cases will be re-simulated under more accurate and specific conditions, once experimental data becomes available later in the project (WP4).

5. ABBREVIATIONS

CERTH	Centre for Research and Technology, Hellas
CFD	Computational Fluid Dynamics
CLC	Chemical looping combustion
CSIC	Spanish National Research Council
CSIC_FI	20 kW _{th} CSIC fuel reactor case with fixed inventory (6 kg)
CSIC-FC	20 kW _{th} CSIC fuel reactor case with fixed circulation flux
CTH	Chalmers University of Technology
FR	Fuel reactor
High_Circ	10 kW _{th} CTH fuel reactor case with double the minimum circulation flux
High_Circ_Pack	10 kW _{th} CTH fuel reactor case with the same circulation as HighCirc, including packings
Low_Circ	10 kW _{th} CTH fuel reactor case with minimum required circulation flux
OC	Oxygen carrier
POC	Post-oxidation chamber
STL	Stereolithography file format
TUDA	Technical University of Darmstadt
TUDA-85	1 MW _{th} TUDA fuel reactor case with fixed inventory of 85 kg
TUDA-160	1 MW _{th} TUDA fuel reactor case with fixed inventory of 160 kg
VD	Volatile distributor

6. REFERENCES

- [1] ANSYS, inc., "ANSYS Fluent User's Guide, Release 2022 R1." Jul. 2021.
- [2] C. K. K. Lun, S. B. Savage, D. J. Jeffrey, and N. Chepur, "Kinetic theories for granular flow: inelastic particles in Couette flow and slightly inelastic particles in a general flowfield," *J. Fluid Mech.*, vol. 140, pp. 223–256, Mar. 1984, doi: 10.1017/S0022112084000586.
- [3] D. Gidaspow, R. Bezburuah, and J. Ding, "Hydrodynamics of circulating fluidized beds: Kinetic theory approach," Jan. 1991, [Online]. Available: <https://www.osti.gov/biblio/5896246>
- [4] C. K. K. Lun and S. B. Savage, "The effects of an impact velocity dependent coefficient of restitution on stresses developed by sheared granular materials," *Acta Mechanica*, vol. 63, no. 1–4, pp. 15–44, Nov. 1986, doi: 10.1007/BF01182538.
- [5] D. G. Schaeffer, "Instability in the evolution equations describing incompressible granular flow," *Journal of differential equations*, vol. 66, no. 1, pp. 19–50, 1987.
- [6] P. C. Johnson and R. Jackson, "Frictional–collisional constitutive relations for granular materials, with application to plane shearing," *J. Fluid Mech.*, vol. 176, no. 1, p. 67, Mar. 1987, doi: 10.1017/S0022112087000570.
- [7] ANSYS, inc., "ANSYS Fluent Theory Guide, Release 2022 R1." Jul. 2021.
- [8] W. Ge *et al.*, "Meso-scale structure—a challenge of computational fluid dynamics for circulating fluidized bed risers," in *9th International Conference on Circulating Fluidized Beds, Hamburg, 2008*.
- [9] A. Nikolopoulos, K. Atsonios, N. Nikolopoulos, P. Grammelis, and E. Kakaras, "An advanced EMMS scheme for the prediction of drag coefficient under a 1.2MWth CFBC isothermal flow—Part II: Numerical implementation," *Chemical Engineering Science*, vol. 65, no. 13, pp. 4089–4099, Jul. 2010, doi: 10.1016/j.ces.2010.03.053.
- [10] M. Zeneli, A. Nikolopoulos, N. Nikolopoulos, P. Grammelis, and E. Kakaras, "Application of an advanced coupled EMMS-TFM model to a pilot scale CFB carbonator," *Chemical Engineering Science*, vol. 138, pp. 482–498, Dec. 2015, doi: 10.1016/j.ces.2015.08.008.
- [11] J. Wang, W. Ge, and J. Li, "Eulerian simulation of heterogeneous gas–solid flows in CFB risers: EMMS-based sub-grid scale model with a revised cluster description," *Chemical Engineering Science*, vol. 63, no. 6, pp. 1553–1571, Mar. 2008, doi: 10.1016/j.ces.2007.11.023.
- [12] A. Klimanek, W. Adamczyk, A. Katelbach-Woźniak, G. Węcel, and A. Szlęk, "Towards a hybrid Eulerian–Lagrangian CFD modeling of coal gasification in a circulating fluidized bed reactor," *Fuel*, vol. 152, pp. 131–137, Jul. 2015, doi: 10.1016/j.fuel.2014.10.058.
- [13] D. Kunii and O. Levenspiel, *Fluidization engineering*, 2nd ed. in Butterworth-Heinemann series in chemical engineering. Boston London Singapore (etc.): Butterworth-Heinemann, 1991.
- [14] A. Abad, J. Adánez, A. Cuadrat, F. García-Labiano, P. Gayán, and L. F. de Diego, "Kinetics of redox reactions of ilmenite for chemical-looping combustion," *Chemical Engineering Science*, vol. 66, no. 4, pp. 689–702, Feb. 2011, doi: 10.1016/j.ces.2010.11.010.
- [15] N. Nemati, Y. Tsuji, T. Mattisson, and M. Rydén, "Chemical Looping Combustion in a Packed Fluidized Bed Reactor—Fundamental Modeling and Batch Experiments with Random Metal Packings," *Energy & Fuels*, vol. 36, no. 17, pp. 9538–9550, 2022, doi: 10.1021/acs.energyfuels.2c00527.
- [16] L. Lu, A. Konan, and S. Benyahia, "Influence of grid resolution, parcel size and drag models on bubbling fluidized bed simulation," *Chemical Engineering Journal*, vol. 326, pp. 627–639, Oct. 2017, doi: 10.1016/j.cej.2017.06.002.
- [17] G. Kanellis *et al.*, "CFD modelling of an indirectly heated calciner reactor, utilized for CO₂ capture, in an Eulerian framework," *Fuel*, vol. 346, p. 128251, 2023.
- [18] ANSYS, inc., "ANSYS Meshing User's Guide, Release 2021 R2." Jul. 2021.
- [19] I. Gogolev, A. H. Soleimanisalim, C. Linderholm, and A. Lyngfelt, "Commissioning, performance benchmarking, and investigation of alkali emissions in a 10 kWth solid fuel chemical looping combustion pilot," *Fuel*, vol. 287, p. 119530, Mar. 2021, doi: 10.1016/j.fuel.2020.119530.